Mode-matching telescopes of the gravitational waves detector Advanced Virgo: installation and characterization.

Author:
Matthieu Laporte (901004-T359)
mlaporte@kth.se

Department of Physics
Royal Institute of Technology (KTH)

Supervisors: Matteo Tacca (APC), Josefin Larsson (KTH)

October 21, 2015

Typeset in LaTeX

ISRN KTH/FYS/––15:79––
SE
ISSN 0280-316X
TRITA-FYS 2015:79

Abstract

The gravitational waves have been theoretically predicted by Einstein in his theory of General Relativity. These gravitational waves interact weakly with matter and are therefore very difficult to detect. However, the gravitational waves emitted by astrophysical sources are expect to contain much information on object which remain unknown such as coalescing binaries and magnetars. Therefore, the detection of gravitational waves is considered as a great scientific challenge nowadays. Large Earth-based interferometer have been built and are currently improved to detect gravitational waves, such as Advanced Virgo. This report will present the work done on a critical part of Advanced Virgo: the mode-matching telescopes. One of these telescope has been tuned during the project and the alignment procedure will be presented. Moreover, several numerical simulations have been performed to evaluate the consequences of a misalignment of the telescope on the beam quality and the conclusions will be presented. In addition, an experiment has been carried out to study the behaviour of a wavefront sensor and of a Fabry-Pérot quality both placed behind an afocal off-axis parabolic telescope.

Final conclusions of the work are that the output mode-matching telescope of Advanced Virgo has been well aligned. The simulations of the errors have allowed to determine the most critical ones (angular position of the largest mirror of the telescope) so that the future tuning procedure will be simplified. These simulations results are in agreement with the experiment and the latter will demonstrate that a wavefront sensor alone will not be sufficient to evaluate the quality of the matching between the beam and the cavity.

Contents

Introduction

0.1 Introduction

The detection of gravitational waves is one of the main challenges of contemporary physics. The gravitational waves are a direct consequence of the Einstein's General Relativity Theory, which connects space and time: distribution of mass energy induces a space-time curvature. In the case of a mass greatly accelerated, the deformations of the space are waves that propagate at the speed of light through the universe: they are gravitational waves. They are emitted by violent astrophysical phenomena such as coalescences of neutron stars or black holes. Their detection will not only allow important tests of General Relativity, but will also open a totally new window onto the Universe, thus providing a new tool for astrophysics and cosmology. Gravitational waves interact weakly with matter and they propagate unaltered along cosmological distances and reach Earth in pristine condition. Thanks to this low interaction, the study of gravitational waves signals can give valuable information not available from the study of electromagnetic waves. Therefore, they give direct access to regions of space that are so far unexplored, for instance the vicinity of very dense objects. In order to detect gravitational waves, the design and the implementation of very sensitive, complex and technologically advanced instruments, able to detect the infinitesimal time varying strains in space-time, are needed [1–5]. Since the available technology was insufficient to assemble instruments with the needed sensitivity, for many years physicists considered impossible to detect gravitational waves, but in the early-1960s possible means of detection have been proposed, followed by the first instruments development. Among the various proposed experimental methods, long baseline optical interferometry is a promising technique for the detection of gravitational waves: Virgo [6] in Europe and LIGO [7] in USA were two large-scale Earth-based Michelson interferometers with Fabry-Pérot cavities in their arms that operated in the last years, which were able to measure very small displacement ($10^{-18} m/\sqrt{Hz}$) and, therefore, to detect the transit of gravitational waves.

Unfortunately, even if Initial Virgo has reached its final sensitivity goal, no gravitational wave detection has been achieved. Therefore, designs of second generation detectors that consist of improvements of the initial ones are being implemented: Advanced Virgo and Advanced LIGO. They aim at increasing the observable event rate by a factor ~ 1000. Moreover, the subsequent largely increased expected event rate widens the possibilities with multi-messenger science. For instance, the joint operation of gravitational wave detectors and high energy neutrinos (HEN) telescopes is particularly appealing since both gravitational waves and HEN travel undisturbed over cosmological distance, escape dense media and are likely to provide an image of the universe complementary to the one given by electromagnetic information. Therefore, coincident observation of

gravitational waves and HEN from the same event could allow a deep investigation of the source.

A group at the *laboratoire Astroparticule et Cosmologie* (APC) is directly involved in the design and in the construction of the second generation gravitational waves detector Advanced Virgo. In particular, it is responsible of the project, the study, the realization, the installation, the tuning and the characterization of the most critical Mode Matching Telescopes installed in the new interferometer [8]. The waist size of the optical beam into the arm cavities is well known (about 1 cm) and it is much different with respect to the one of the beams respectively generated at the output of the laser source and detected by the exploited photodiodes. At the input of the interferometer one telescope is essential in order to adapt the dimension of the beam to the cavities of the interferometer. In the same way, on the output benches (in transmission of the end mirrors of the Fabry-Pérot cavities and at the detection of the interference signal) some telescopes are needed to reduce the dimension of the beam in order to send them on cameras and photodiodes. For all the telescopes the two main sources of the degradation of the beam quality are the optical aberrations (spherical aberration, coma, astigmatism) and the scattered light. They should be very low in order not to introduce noise, which can affect the interferometer sensitivity.

The two main and more critical telescopes of the whole experiment are installed respectively on the *Suspended Input Optics Bench* and on the *Suspended Output Optics Bench*, which are quite compact with respect to the huge amount of optical elements that they should include. Therefore, these telescopes should be very compact and light, even if they should provide a large magnification factor. The final design of these telescopes foresees three elements, two parabolic mirrors in an off-axis configuration, thus very hard to properly align, and a meniscus lens installed on the suspended benches.

0.2 Outline of the Thesis

This report will present the theoretical context of the gravitational waves and their sources in a first part. In a second part, the interferometric detection of gravitational waves principles are detailed. The third part contains a description of the initial Virgo and Advanced Virgo. Finally the fourth part is dedicated to the work on the mode-matching telescopes of Advanced Virgo.

0.3 Author's Contribution

I worked six months in the Virgo team at the APC. The first part of my work consisted in tuning the off-axis parabolic telescope installed on the bench at the output of the interferometer, before the latter would be suspended in its vacuum chamber at the Virgo site in Cascina (Italy). The second part of my work consisted in evaluating the consequences of a detuning of the telescope on the beam quality at the output, particularly for the matching on an optical cavity placed behind it. This evaluation was made with numerical simulations on a dedicated software. The conclusions of these simulations will help the future remote tuning of the telescope when it will be suspended under vacuum. It gives indeed a qualitative and quantitative evaluation of the consequences on the beam quality for every degrees of freedom likely to be detuned during the suspension

and vacuum process. The third part of my work was to correlate the signals given by two different sensors when the telescope is misaligned. This was achieve experimentally in the laboratory. The two different sensors are a wavefront analyser that will measure the beam properties after the telescope and a photodiode that will measure the signal at the output of an optical cavity placed behind the telescope. This photodiode allows to evaluate the matching of the beam with the cavity by comparing the intensity of the fundamental Gaussian mode to the intensity of the higher order matching mode.

Chapter 1

Gravitational waves and their sources

1.1 Gravitational waves

In the theory of General Relativity by Einstein, the gravitational interaction is defined as a geometric effect of curvature of space-time [9]. In this geometric theory of gravitation, gravitational waves appear to be local deformations of space-time propagating at a finite velocity that are emitted by massive accelerated body. The coupling between gravitational radiation and matter is predicted to be extremely weak, therefore only the gravitational waves emitted by notably massive and compact astrophysical sources that are accelerated at relativistic velocities are expected to have detectable amplitudes. As a consequence, one cannot expect to produce detectable gravitational waves in laboratory, therefore the detectors aim at detecting gravitational waves emitted by astrophysical sources, travelling through the vicinity of Earth.

1.1.1 Einstein equations and its Wave solution

The gravitational field, and therefore the space-time curvature, is determined by the energy-matter distribution given by the Einstein equations:

$$G_{\mu\nu} = R_{\mu\nu} - \frac{1}{2} g_{\mu\nu} R = \frac{8\pi G}{c^4} T_{\mu\nu} \quad (\mu, \nu = 0, 1, 2, 3), \tag{1.1}$$

where G is the Newton's constant of gravitation and c the speed of light. $G_{\mu\nu}$ is the Einstein tensor, which describes the space-time geometry. R is the scalar curvature. $R_{\mu\nu}$ and $g_{\mu\nu}$ are two symmetric tensors, respectively the so-called Ricci tensor and the metric tensor. The Ricci tensor derives from the contraction of the Riemman tensor (or *curvature tensor*) $R^{\alpha}_{\beta\mu\nu}(\alpha, \beta, \mu, \nu = 0, 1, 2, 3)$ with the metric tensor:

$$R_{\mu\nu} = g^{k\alpha} R_{k\mu\alpha\nu} = R^{\alpha}_{\mu\alpha\nu} \quad (\alpha, k, \mu, \nu = 0, 1, 2, 3). \tag{1.2}$$

The Riemann tensor, or *curvature tensor*, $R^{\alpha}_{\beta\mu\nu}$ tells how much a vector is transformed when it is parallel transported around a loop in a curved space-time, thus it is said to hold the information of the curvature of space-time.

Finally, $T_{\mu\nu}$ is the *stress-energy tensor* describing the two sources of the gravitational field: energy and matter. It is a symmetric tensor.

The Einstein equations constitute a set of non-linear equations. A way to solve them consists in adopting a perturbative approach, considering the limit of weak gravitational field in vacuum. The metric is then written as:

$$g_{\mu\nu} = \eta_{\mu\nu} + h_{\mu\nu} \ , \tag{1.3}$$

where $\eta_{\mu\nu}$ is the flat Minkowski space-time metric tensor and $h_{\mu\nu}$ is the small gravitational perturbation ($|h_{\mu\nu}| << 1$).With these considerations, one can demonstrate that the solution propagates in space-time like a wave: a gravitational wave. Thanks to the freedom in the choice of coordinate system, a gauge where $h_{\mu\nu}$ is traceless and transverse can be chosen (TT gauge), which allows to simplify (1.1) into:

$$\left(\nabla^2 - \frac{1}{c^2}\frac{\delta^2}{\delta t^2}\right) h_{\mu\nu} = 0 \ , \tag{1.4}$$

which describes the propagation of a wave at speed c. Solutions of the equation (1.4) can be written as plane waves:

$$h_{\mu\nu} = \epsilon_{\mu\nu} exp[i(\Omega t - \vec{k}.\vec{x})] \tag{1.5}$$

with angular frequency Ω , wave vector $\vec{k}$, and polarization tensor $\epsilon_{\mu\nu}$. The latter, for a wave propagating along the z direction in the TT gauge, can be written as:

$$\epsilon_{\mu\nu} = h_+ \epsilon^+_{\mu\nu} + h_\times \epsilon^\times_{\mu\nu} \ , \tag{1.6}$$

where h_+ and $h_\times$ are the coordinates in the basis $\left\{\epsilon^+_{\mu\nu}; \epsilon^\times_{\mu\nu}\right\}$, and the basis tensors are:

$$\epsilon^+_{\mu\nu} = \begin{pmatrix} 0 & 0 & 0 & 0 \\ 0 & 1 & 0 & 0 \\ 0 & 0 & -1 & 0 \\ 0 & 0 & 0 & 0 \end{pmatrix} \qquad and \qquad \epsilon^\times_{\mu\nu} = \begin{pmatrix} 0 & 0 & 0 & 0 \\ 0 & 0 & 1 & 0 \\ 0 & 1 & 0 & 0 \\ 0 & 0 & 0 & 0 \end{pmatrix} \ .$$

Consequently, the gravitational waves has only two possible polarization states noted $+$ and $\times$.

1.1.2 Emission of gravitational waves

Electromagnetic waves are emitted by accelerated charges and their emission is linked to the electromagnetic multipole. In the same way, gravitational waves are emitted by accelerated masses and their emission is linked to the gravitational multipole. Unlike electromagnetism though, the gravitational dipole is null due to the conservation of the total momentum of isolated systems. As a consequence, gravitational waves have a quadrupole nature. Emission of gravitational waves is related to the variations of the quadrupole moment of the mass distribution tensor Q_{ij} $(i, j = 1, 2, 3)$:

$$Q_{ij}\left(t, \vec{x}\right) = \frac{1}{c^2}\int_V T_{00}\left(t, \vec{x}\right) x_i x_j \mathrm{d}V \ . \tag{1.7}$$

$T_{00}(t, \vec{x})$ is the time component of the stress-energy tensor. It appears that symmetric spherical mass distributions, whose quadrupole moment is zero, do not emit gravitational waves.
Far from the source and for velocities much smaller than the speed of light (i.e. in the far field and slow motion approximation), the amplitude of the wave generated by the quadrupole moment can be written as:

$$h_{ij} = \frac{2}{r}\frac{G}{c^4}\frac{\partial^2}{\partial t^2}Q_{ij}\left(t - \frac{r}{c}, \vec{x}\right) \ , \tag{1.8}$$

where r is the distance source - point of observation and $t - \frac{r}{c}$ is the delayed time at which the wave reaches the point of observation. The factor $\frac{G}{c^4} \simeq 8.10^{-45} s.kg^{-1}$ is extremely small. In fact, it is so small that one can demonstrate that it is impossible to generate gravitational waves with a controlled source in laboratory. Thus, astrophysical sources are the only sources to be studied for the detection of gravitational waves.

1.2 Astrophysical sources of gravitational waves

Three categories of gravitational sources can be distinguished according to the time evolution of their emission:

- **Periodic or quasi-periodic sources**. Sources emitting gravitational waves at a quasi constant frequency during the time of observation fall under this category. It is the case for pulsating neutron stars (pulsars) and coalescing binaries during the early phase of the process.
- **Bursts sources**. These sources emit gravitational waves over a time smaller than the duration of observation. They involve violent gravitational collapsing such as magnetars, supernovae or coalescing binaries at their merging point.
- **Stochastic background**. It is the statistically fluctuating background signal, of astrophysical and cosmological origins.

1.2.1 Coalescing binaries

Binary systems are among the best presently known stellar objects. A binary system consists in two star-like bodies orbiting around each other. If the two stellar objects are compact bodies such as a pair of neutron stars, a pair of black holes or a pair black hole - neutron star, the system is expected to emit a large amount of energy through gravitational radiation at a frequency equal to the double of the orbital frequency. Such a system has an orbital motion that can be divided into three different phases as illustrated in Figure 1.1:

- In the early phase, the orbits are wide and the emission is of small amplitude with a low frequency of the order of mHz. Such a low frequency cannot be detected on Earth, where the signal would be drown in the seismic noise.
- As the system loses energy, the two stars get closer. The amplitude of the gravitational radiation increases as well as its frequency. This phase is called *coalescence*.

- Finally, the motion ends when the two stars start to merge. This event is violent and expected to emit a gravitational burst.

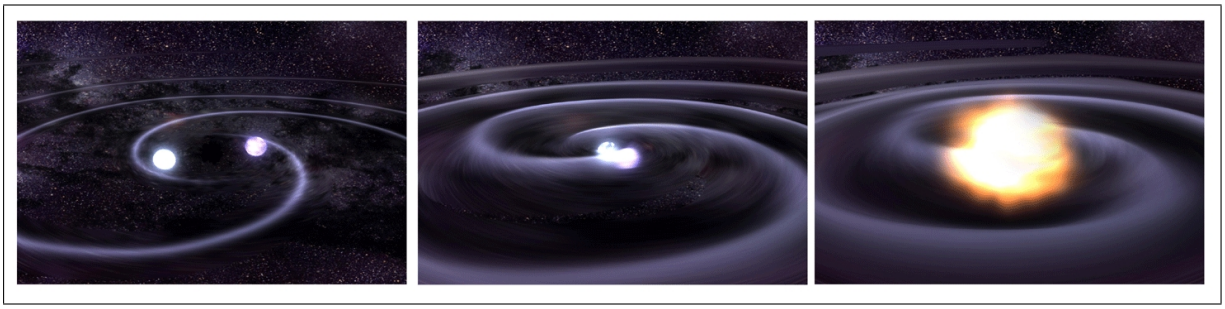

Figure 1.1: Artist's impression of an coalescing binary during its different phases. Figure taken from [20]

Those sources are well identified. A detection of gravitational waves emitted by coalescing binaries would be a validation of the General Relativity theory. When a neutron star merges with a black hole, the emitted gravitational waves are expected to hold precious information on the internal structure of neutron stars. Moreover, the coalescence of two neutron stars is a candidate to explain the γ-ray bursts phenomena observed in distant galaxies. Therefore, detecting a gravitational wave in coincidence with such a burst would be a perfect test for these mechanisms.

1.2.2 Pulsars

Pulsars are a particular type of neutron stars. They are rotating very fast, leading to periodic electromagnetic pulse emissions with a period corresponding to the rotation period of the pulsar. Most of them emits in the radio frequency domain, except for few of them emitting in the visible band. 1500 radio pulsars are known, with rotation periods from one millisecond to few seconds. If a mass asymmetry would exist at the surface of a pulsar, it could emit gravitational waves at twice the rotation frequency.

1.2.3 Magnetars

Magnetars are little known stellar objects. They seem to be isolated neutron stars producing extreme magnetic fields ($10^{15}G$). Two very rare types of objects could fit into that description: soft gamma repeaters and X-ray pulsars. They are compact sources of X-ray, randomly emitting soft gamma rays bursts. They are thought to emit gravitational waves bursts, but the lack of theoretical understanding cannot provide good order of magnitude of the expected amplitude of these bursts.

1.2.4 Supernovae

Gravitational waves emission from a Supernova happens during the gravitational collapse of the star. The amplitude of the radiation directly depends on the asphericity of the collapse. The detection rate of such event is difficult to estimate. The Supernova rate in the local group of galaxy (up to 300 kpc from Earth) is rather low (1 event per two

decades), while it might happen once every other year between 3 and 5 Mpc from Earth. Since no proper theoretical model of Supernova event exists, the features of the emitted gravitational waves are difficult to predict. It is however expected to be burst-like, with few milliseconds durations.

1.2.5 Stochastic background

Two different components of such a stochastic background could be distinguished. The first one is the incoherent superposition of all emitted gravitational waves by too numerous, faint and distant sources to be resolved. Secondly, cosmological models predict a stochastic background generated during the early age of the Universe [10]. It is thought to be isotropic, unpolarized and stationary. The spectrum of such a background would carry information on the Universe at $\sim 10^{-20}$ - $\sim 10^{-26}$ seconds old.

Chapter 2

Interferometric detection of gravitational waves

2.1 Geodesic deviation

To detect gravitational waves, one has to consider a system with at least two particles. Let δx^λ be the distance between two probe particles. The effect of a gravitational wave passing through such a system is described by the geodesic deviation:

$$\frac{d^2\delta x^\lambda}{d\tau^2} = R^\lambda_{\nu\beta\mu}\frac{d\delta x^\beta}{d\tau}\frac{d\delta x^\nu}{d\tau}\delta x^\mu \ . \tag{2.1}$$

The relative acceleration thus depends on the curvature tensor $R^\lambda_{\nu\beta\mu}$. If a gravitational wave $h_{\mu\nu}$ perturbs a flat space-time metric (i.e. $g_{\mu\nu} = \eta_{\mu\nu} + h_{\mu\nu}$), equation 2.1 can be written as:

$$\frac{d^2\delta x^\lambda}{d\tau^2} = \frac{1}{2}\eta^{\lambda i}\frac{\mathrm{d}^2 h_{im}}{\mathrm{d}t^2}\delta x^m \quad (i,m = 1,2,3). \tag{2.2}$$

The solution of such an equation can be written as:

$$\delta x^\lambda = \delta x^\lambda_0 + \frac{1}{2}\eta^{\lambda i}h_{ik}\delta x^k_0. \tag{2.3}$$

which is the sum of an unperturbed term δx^λ_0 and a term representing the perturbation induced by the gravitational wave. As a consequence the relative distance between the two bodies varies in time according to the oscillatory perturbation of the gravitational wave. This effect is depicted in Figure 2.1

2.2 Michelson interferometers

In order to detect gravitational waves, the distance variation between two bodies has to be measured. A good way to detect such variations of distances is to use laser interferometry. The basic configuration for gravitational waves detectors is the Michelson interferometer [11], [12]. It consists of a source of coherent light (usually a laser), a beamsplitter and two mirrors along two orthogonal directions, equally distant from the beamsplitter. The laser beam that comes from the source is divided in two parts by the beamsplitter. Each

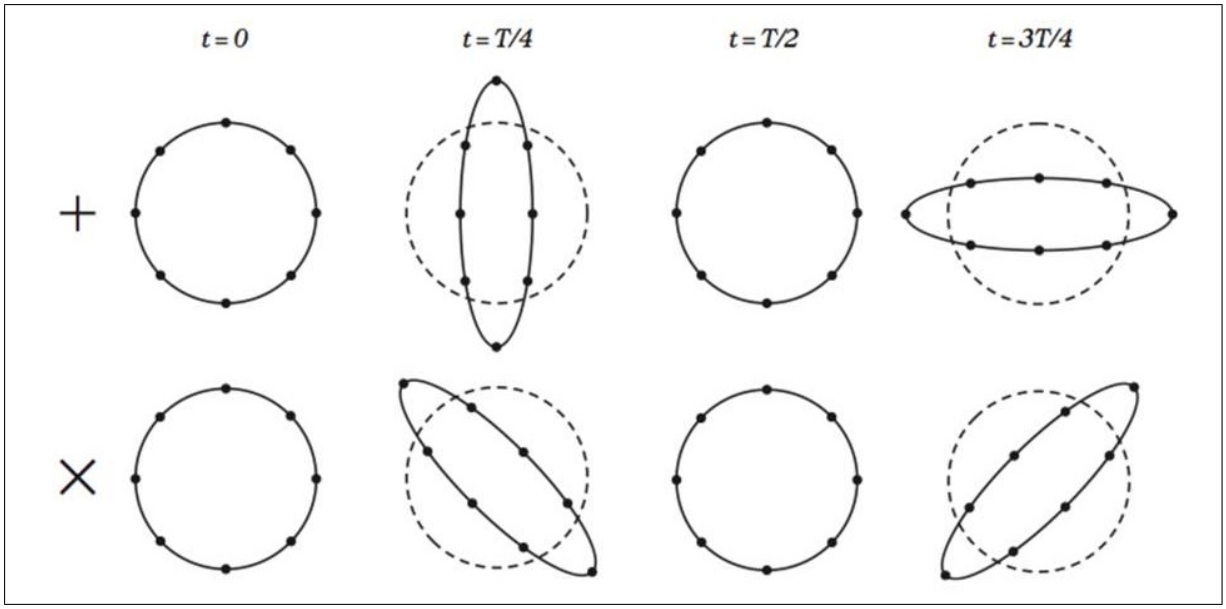

Figure 2.1: Representation of the effect of a gravitational wave on a set of free-falling particles for the two polarisation × and +. T is the period of the gravitational wave. Figure taken from [21]

part is then reflected by the mirrors and the two parts recombine at the beamsplitter. The optical configuration of a Michelson interferometer is depicted in Figure 2.2.

The Michelson interferometer measures the phase difference between the two beams propagating in the two arms. That phase is related to the difference of path length between the two arms, or the difference between the propagation times in the two arms.

Let ψ_{in} be the input field at the beamsplitter, ψ_{out} be the output field of the interferometer, r_i and t_i respectively the amplitude reflectivity and amplitude transmissivity of the two mirrors and the beamsplitter ($i = 1, 2, BS$), and $k = \omega/c = 2\pi/\lambda$ the wave number.

In the two different paths, the beam undergoes a reflexion and a transmission on the beamsplitter, a reflexion on the end mirror and two propagations along the arm length L_i. Thus the output field can be written as:

$$\begin{aligned}\psi_{out} &= t_{BS}e^{-ikL_1}(-r_1)e^{-ikL_1}(-r_{BS})\psi_{in} + (-r_{BS})e^{-ikL_2}(-r_2)e^{-ikL_2}t_{BS}\psi_{in} \\ &= t_{BS}r_{BS}\left(r_1e^{-i2kL_1} + r_2e^{-i2kL_2}\right)\psi_{in}\ .\end{aligned}$$

The output power can be written as:

$$P_{out} = P_{in}T_{BS}R_{BS}\left(R_1 + R_2 + 2r_1r_2\cos\phi\right) \tag{2.4}$$

where $R_i = |r_i|^2$, $T_i = |t_i|^2$ and $\phi = 2k(L_2 - L1)$. The maximum and minimum output power can be easily defined as, respectively, $P_{max} = P_{out}(\phi = 0)$ and $P_{min} = P_{out}(\phi = \pi)$. The contrast C of the Michelson interferometer can be define as:

$$C = \frac{P_{max} - P_{min}}{P_{max} + P_{min}} = \frac{2r_1r_2}{R_1R_2}\ . \tag{2.5}$$

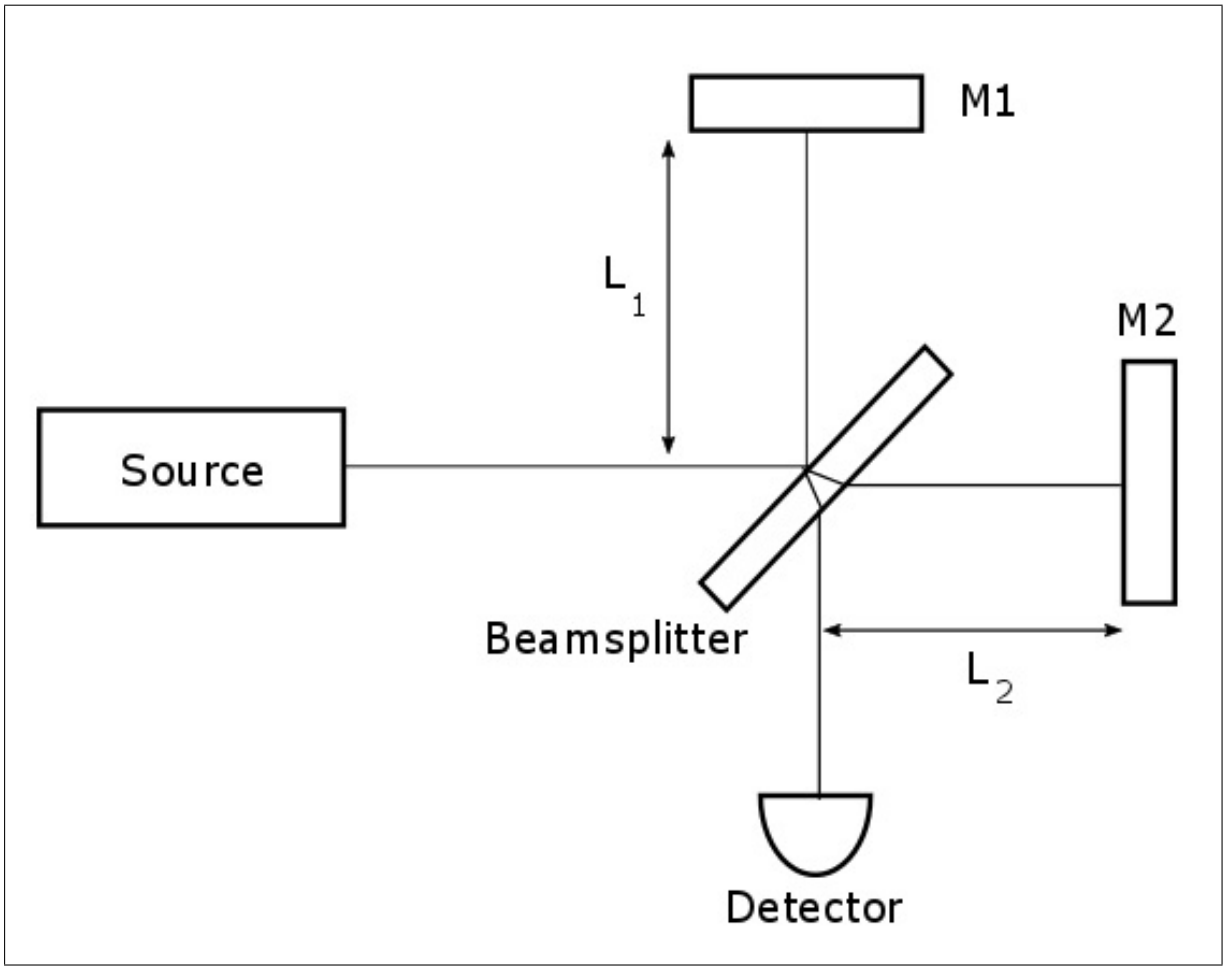

Figure 2.2: Scheme of a basic Michelson interferometer

The output power can then be rewritten as:

$$P_{out} = P_{in} T_{BS} R_{BS} \left(R_1 + R_2\right) \left(1 + C \cos \phi\right) \ . \tag{2.6}$$

The output power, that can be measured by a photodiode, depends on changes in the arms lengths. Assuming that the two end mirrors act like free-falling masses, an incident gravitational wave would contract the length of one arm and expand the length of the other arm. Thus, the output power would be modulated by the passage of the wave.

2.3 Noise sources

Due to the low amplitude of the gravitational waves, the output signal of the gravitational wave interferometer is extremely affected by noises of various origins. The fundamental noises affecting the signal are the following:

- **Shot noise**. This noise comes from the quantum nature of light. The photons hit the detector randomly, following a Poisson law, resulting in fluctuations in the signal.
- **Fluctuation of the radiation pressure on the mirrors**. Each photon hitting a mirror exerts a slight pressure on it. It results in slight fluctuating modifications of the optical path.
- **Seismic noise**. Internal activity of the Earth produces ground vibration. Even with the best filters, there is still some seismic noise due to seismic activity at low frequencies.
- **Local fluctuations of the Newtonian gravitational field in the detector**. They are induced by the time variation of the mass density distribution around the detector caused by seismic waves, sound waves or temperature perturbation in the air.
- **Local thermal fluctuations on the mirrors**. The coating on the mirrors are subjects to temperature fluctuations that modify their optical properties.

There is also a set of technical noises :

- Fluctuation of the laser beam in amplitude, frequency and position.
- Diffused stray light that re-couple with the signal.
- Electronic noise in read-out and control systems, which is similar to shot noise.

2.4 Sensitivity improvements

The sensitivity of the detector, which can be defined as the smallest signal that can be distinguished from noises, depends directly on the power of the input beam and the arms length. The arm length for a ground detector is limited to a few kilometres. The lasers meeting the requirements for such detectors can reach 200 W.

It is possible to increase the effective path travelled by the beam by using resonators. If Fabry-Pérot cavities are placed in the arm of the interferometer, the light travels back and forth inside the cavities, increasing the optical path by the cavity length times the number of round trips.

The Michelson interferometer dedicated to gravitational waves detection operates in the dark fringe configuration. The interference at the output is destructive, thus the power is mainly reflected towards the laser. Therefore, another improvement solution is to use a power recycling cavity: a mirror is added before the beamsplitter, forming a resonator with the first mirrors of the two arms cavities that re-inject the light in the interferometer.

Finally, the beam jitter, amplitude noise and frequency noise of the laser can be filtered with a mode-cleaner cavity. Such a cavity can also be placed at the output, to filter the signal and increase the signal-to-noise ratio.

All these possible improvement are shown in figure 2.3 and will be detailed.

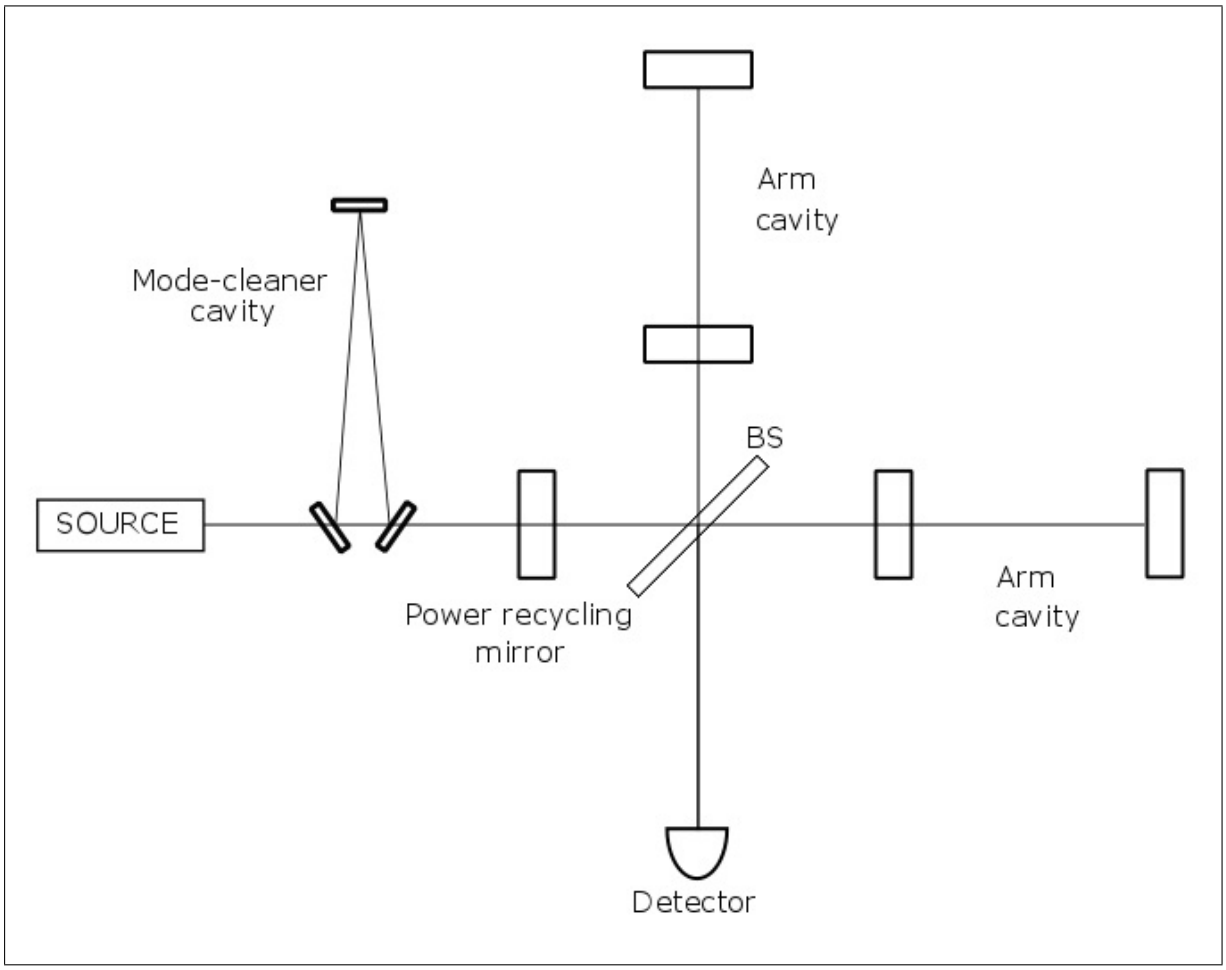

Figure 2.3: Michelson interferometer improved with arm cavities, power recycling cavity and input mode-cleaner.

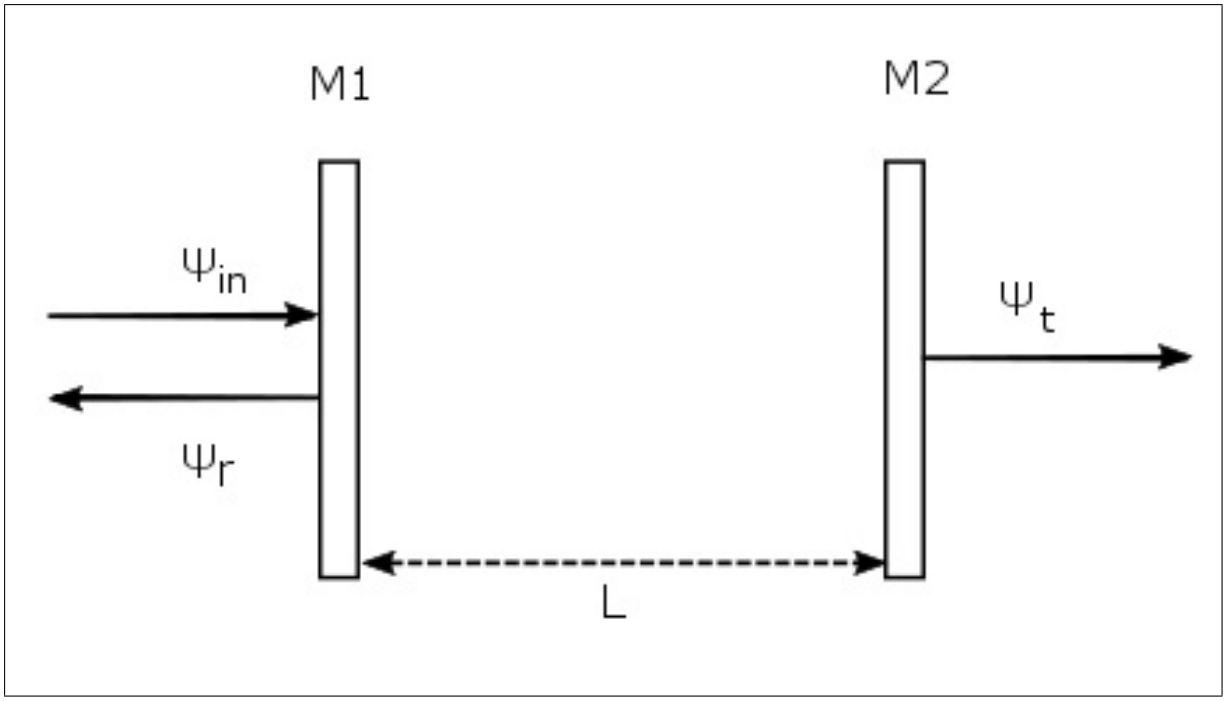

Figure 2.4: Scheme of a simple Fabry-Pérot cavity

2.4.1 Fabry-Pérot arm cavity

In a simple Fabry-Pérot cavity, two mirrors $M1$ and $M2$ are separated by a distance L, as depicted in Figure 2.4. The input signal is a field ψ_{in} with a wavelength λ. The phase accumulated during a single trip in the cavity is $\phi = 2\pi L/\lambda$.

The first transmitted light at the output, $\psi_{t,0}$ is given by:

$$\psi_{t,0} = \psi_{in} t_1 t_2 e^{i\phi} \tag{2.7}$$

thus the n^{th} transmitted light $\psi_{t,n}$ is :

$$\psi_{t,n} = \psi_{t,0} \left(r_1 r_2 e^{i2\phi}\right)^n \tag{2.8}$$

A Fabry-Pérot cavity only operates if $|r_1| \neq 1$ therefore $|r_1 r_2 e^{i2\phi}| < 1$ and the total transmitted light ψ_t can be written as:

$$\psi_t = \psi_{t,0} \sum_{n=0}^{+\infty} \left(r_1 r_2 e^{i2\phi}\right)^n = \psi_{in} \frac{t_1 t_2 \exp(i\phi)}{1 - r_1 r_2 \exp(i2\phi)} \ . \tag{2.9}$$

In terms of power:

$$P_t(\phi) = |\psi_t|^2 = P_i n \left(\frac{t_1 t_2}{1 - r_1 r_2}\right)^2 \frac{1}{1 + \dfrac{4 r_1 r_2}{1 - r_1 r_2} sin^2\phi} \ . \tag{2.10}$$

The cavity is said to be resonant when $\phi = k\pi$ ($k \in \mathbb{Z}$). In that case the incident light interferes constructively with the stored light in the cavity and the output power is maximum.

The separation between two consecutive resonance points is called the Free Spectral Range (FSR). It is equal to $\frac{c}{2L}$ in term of frequency and $\frac{\lambda}{2}$ in terms of wavelength.

Another characteristic number is the cavity *finesse*. It is defined as the ratio between the free spectral range and the full width at half maximum (FWHM):

$$\mathcal{F} = \frac{\text{FSR}}{\text{FWHM}} = \frac{\pi\sqrt{r_1 r_2}}{1 - r_1 r_2} \tag{2.11}$$

In the case of an arm cavity in a Michelson interferometer, we are interested in the reflected field ψ_r. With a similar reasoning, we have:

$$\psi_{r,0} = -\psi_{in} t_1^2 r_2 e^{2i\phi} \tag{2.12}$$

and then, taking the reflection on $M1$ into account:

$$\psi_r = -r_1\psi_{in} - \psi_{in}\frac{r_2 t_1^2 \exp(2i\phi)}{1 - r_1 r_2 \exp(2i\phi)} = \psi_{in}\frac{r_1 - r_2(t_1^2 + r_1^2)\exp(2i\phi)}{1 - r_1 r_2 \exp(2i\phi)} \tag{2.13}$$

When $r_1 - r_2(t_1^2 + r_1^2) = 0$, the reflected field at a resonance point in null. This situation is called *optimal coupling*.

For small phase shift around the resonance, the phase variation of the reflected field is given by:

$$\frac{d\phi_r}{d\phi} = \frac{d}{d\phi}\arg\left(\frac{\psi_r}{\psi_{in}}\right) = r_2\frac{(t_1^2 + r_1^2) - r_1^2}{(1 - r_1 r_2)(r_1 + r_2(t_1^2 + r_1^2))} \ . \tag{2.14}$$

If $M1$ has no loss, i.e. $(t_1^2 + r_1^2) = 1$, and $r_1 \sim r_2 \sim 1$, this simplifies to:

$$\frac{d\phi_r}{d\phi} \simeq \frac{2\mathcal{F}}{\pi} \ . \tag{2.15}$$

This result shows that for a small detuning around the cavity resonance, like the one induced by an impinging gravitational wave, the phase shift of a reflected beam at a Fabry-Pérot arm cavity is amplified by a factor proportional to the finesse of the cavity. Since this phase shift is also proportional to the arm length, this is equivalent to an amplification of the effective optical path travelled by the beam. This effective optical path can be written as:

$$L_{eff} = \frac{2\mathcal{F}}{\pi} L \ . \tag{2.16}$$

2.4.2 Power recycling

Let us consider a Michelson interferometer in the destructive interference condition. If the end mirrors have a high reflectivity, almost all the power is sent back to the laser. This power can be stored in the detector by adding a semi-reflective mirror between the source and the beamsplitter. It would form a cavity together with the rest of the interferometer, considered as a composite mirror with a resulting reflectivity r_{ITF}.

The field inside the power recycling cavity ψ_{res} can be easily computed in the simple case where the power recycling mirror is coupled with only one Fabry-Pérot arm cavity:

$$\psi_{res} = \psi_{in}\frac{t_{PR}}{1 - r_{PR} r_{FP} \exp(2i\phi_{PR})} \ , \tag{2.17}$$

where t_{PR} and r_{PR} are the power recycling mirror transmitivity and reflectivity, respectively, $r_{FP} = \dfrac{r_1 - r_2(t_1^2 + r_1^2)\exp(2i\phi_{FP})}{1 - r_1 r_2 \exp(2i\phi_{FP})}$ is the equivalent reflectivity of the Fabry-Pérot arm cavity. ϕ_{PR} and ϕ_{FP} are the phases acquired in the power recycling cavity and the arm cavity, respectively. The coupled cavities are in double resonance when both $\phi_{PR} = n\pi$ and $\phi_{FP} = m\pi$ $(n, m \in \mathbb{Z})$.

2.4.3 Mode-cleaner cavities

The Laser source produces frequency and amplitude noises along with jitter. Those noises can be filtered by a mode-cleaner cavity tuned to optimal coupling for the transmission of the input beam [13]. It acts like a low-pass filter for the amplitude and frequency noises, with a cut-off frequency $f = 1/4\pi\tau_s$ where τ_s is the storage time of the cavity, defined by:

$$\tau_s = \frac{2L}{c}\frac{\sqrt{r_1 r_2}}{1 - r_1 r_2} \tag{2.18}$$

The beam jitter leads to the production of higher order laser modes by the source. The mode-cleaner cavity reflects them, as they are not in resonance. Mode-cleaner cavities can be placed at the input or at the output of the interferometer.

Chapter 3

Virgo and Advanced Virgo

3.1 Virgo, a first generation detector

3.1.1 The Virgo initial optical layout

Virgo was an Earth-based Fabry-Pérot Michelson interferometer which used also the power recycling methods previously described. Its arms (called North arm and West arm), are 3 km long Fabry-Pérot cavities. The input mirrors of the cavities are separated from the beamsplitter by approximately 6 meters. The power recycling mirror is also approximatively 6 meters before the beamsplitter.

The laser source produces a beam with a continuous power of about 20 W at $\lambda = 1064\ nm$. It is generated by a high-stability Nd:YAG master laser coupled with a $Nd : YVO_4$ slave laser which delivers the high power. Before entering the interferometer, the beam goes through the so-called *Input Mode-Cleaner* cavity (IMC). It consists in a triangular cavity, 144 meters long with a finesse $\mathcal{F} \simeq 1000$. This cavity is used to filter the beam jitter of the source, but it also acts as an active frequency stabilization device. Then the beam passes the power recycling mirror (PR) which has a reflectivity $R = 92\%$. The beamsplitter (BS) splits the beam equally and each part goes through the two cavities. Originally, both arm cavities had input mirrors with a reflectivity $R = 88\%$ and end mirrors with a reflectivity $R \simeq 1$ leading to a finesse $\mathcal{F} \simeq 50$ for both arm cavities. A first improvement on the input mirrors have raised the reflectivity to $R = 96\%$, leading to a finesse $\mathcal{F} \simeq 150$.

The mirrors used in the original Virgo were made of high quality fused silica. The power recycling mirror, along with the cavities mirrors, weighed 21 kg, for a 35 cm diameter. The beam splitter was significantly smaller: 23 cm diameter for 5 kg.

3.1.2 Infrastructure

The very high sensitivity needed can only be reached if the interferometer is placed in high vacuum. Moreover, a complex filtering system needs to be built to filter the seismic noise. All the mirrors are therefore suspended to structures that isolate them from the ground seismic noises. The mirrors and their suspensions are placed in vacuum towers, and those towers are linked by smaller vacuum pipes where the laser beam passes.

3.2 Advanced Virgo

Even though Virgo has reached its extreme goal sensitivity (a displacement noise spectral density of 10^{-18} $m/\sqrt{Hz}$), a gravitational wave detection has not been achieved since the rate of the involved astrophysical events was too low. Therefore, a new generation of gravitational waves detectors (Advanced Virgo [14] and Advanced LIGO [15]) has been studied and it is now under construction. The goal of the Advanced detectors is to extend the distance at which a target source can be detected by a factor ~ 10, which corresponds to increase the event rate by a factor ~ 1000 with respect to the detectors of the first generation. The final sensitivity goal will be gradually reached [16]: as the sensitivity improves, the detection rate, as well as the source localization capability, will improve. The improved sensitivity of the Advanced detectors suggests that a gravitational wave detection could be possible in the next few years.

3.2.1 Improvements

Here are the main improvements of Advanced Virgo compared to initial Virgo [14]:

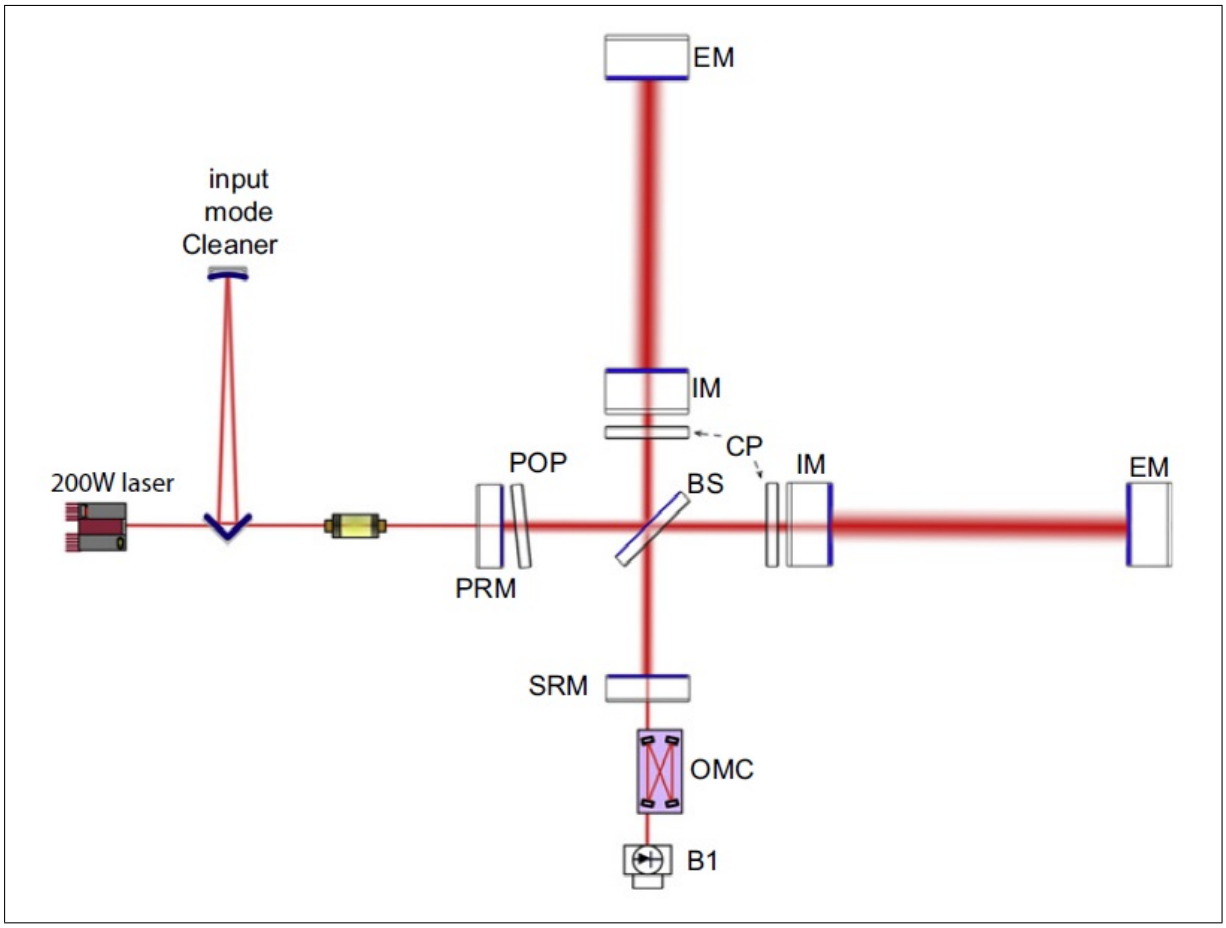

Figure 3.1: A simplified scheme of the optical layout of Advanced Virgo. Figure taken from [14]

optical configuration Figure 3.1 shows the simplified optical layout of Advanced Virgo (AdV).

Advanced Virgo is a dual-recycled Michelson interferometer. A signal recycling cavity is placed in the interferometer, besides the power recycling cavity. It consists in a signal recycling mirror installed between the beamsplitter and the output mode-cleaner. The signal recycling cavity has tunable parameters, allowing to optimize the sensitivity for different sources of gravitational waves. The finesse of the Fabry-Pérot cavities is increased up to 443. The beam spot size has been increased on the mirrors, in order to reduce thermal noise on the mirrors coating. Having larger beam implies having new telescopes to achieve mode-matching on the arm cavities and the output mode-cleaner cavity. The output mode-cleaner cavity (OMC) has been changed. It consists of two identical bow-tie cavities placed in series. Each one is a monolithic fused silica block. Such a compact design allows to limit the cavity length noise. Its round trip length is 248 mm and it has a finesse of 143.

laser power To improve the sensitivity at high frequency, the laser power is increased. The reference level, on which the reference sensitivity is based, is 125 W after the input mode-cleaner. It corresponds to a laser power of 175 W at the source, considering the loss in the injection system. At the beginning of the operations a lower laser power will be used.

thermal control system Higher laser power also means higher thermal lensing effects. Besides increasing the spot size, a complex thermal compensation system is built. CO_2 laser will shine on compensation plates placed before the input mirrors of the arm cavities. By heating those plates, the thermal lensing effect can be coped with. Moreover, ring heaters placed around mirrors can be used to modify their radius of curvature. Such systems also implies the use of sensors and cameras to measure the variations of the radii of curvature and of the thermal lensing.

Mirrors Higher laser power also means higher radiation pressure. To counter this effect, the AdV mirrors are twice as heavy (42 kg) compared to the Virgo mirrors. The most critical are made of ultra high homogeneity fused silica. They achieved a flatness $< 0.5\ nm\ rms$ thanks to state of the art polishing techniques.

Stray light control Part of the light in the interferometer can be back-scattered and pollute the signal and therefore the sensitivity of the detector. To cope with this problem, baffles are installed in the interferometer, either suspended around the mirrors or connected to the ground inside the vacuum links.

3.2.2 Sensitivity goals

Figure 3.2 shows the sensitivity reference curve of advanced Virgo along with all the limiting noises. The quantum noise is the main limiting source of noise at frequency $> 300\ Hz$. For lower frequency, $< 50\ Hz$, the sensitivity is limited by the sum of quantum noise, magnetic noise, the thermal noise in the suspension and the gravity gradient, mainly. For the frequency range $50 < f < 300\ Hz$, the limiting noise is mainly the coating Brownian thermal noise of the optics.

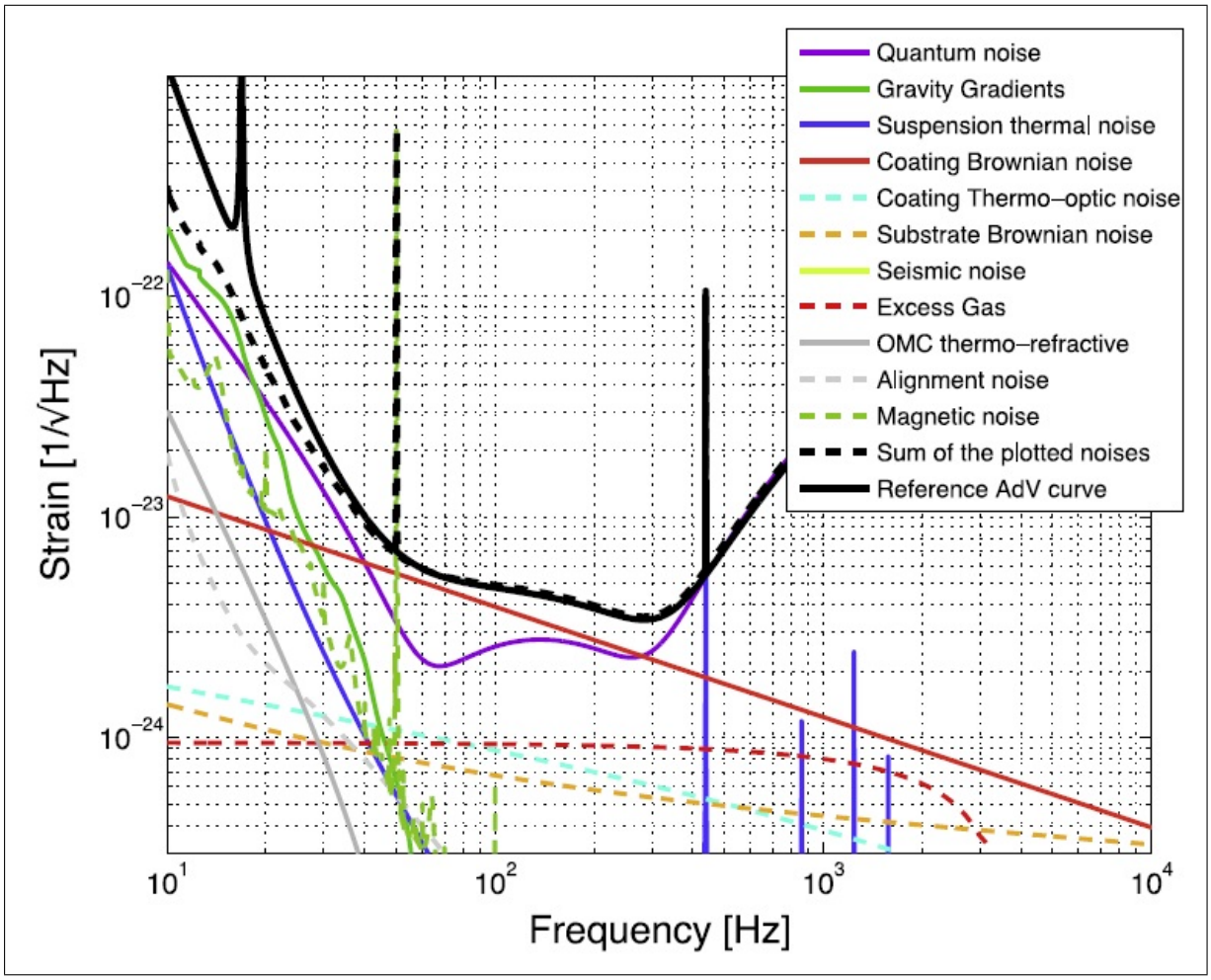

Figure 3.2: The Advanced Virgo design sensitivity curve and its reference noise Budget. Figure taken from [14]

Figure 3.3 shows three sensitivity curves of Advanced Virgo for three different operating regimes and, in comparison, the sensitivity curve of the initial Virgo.

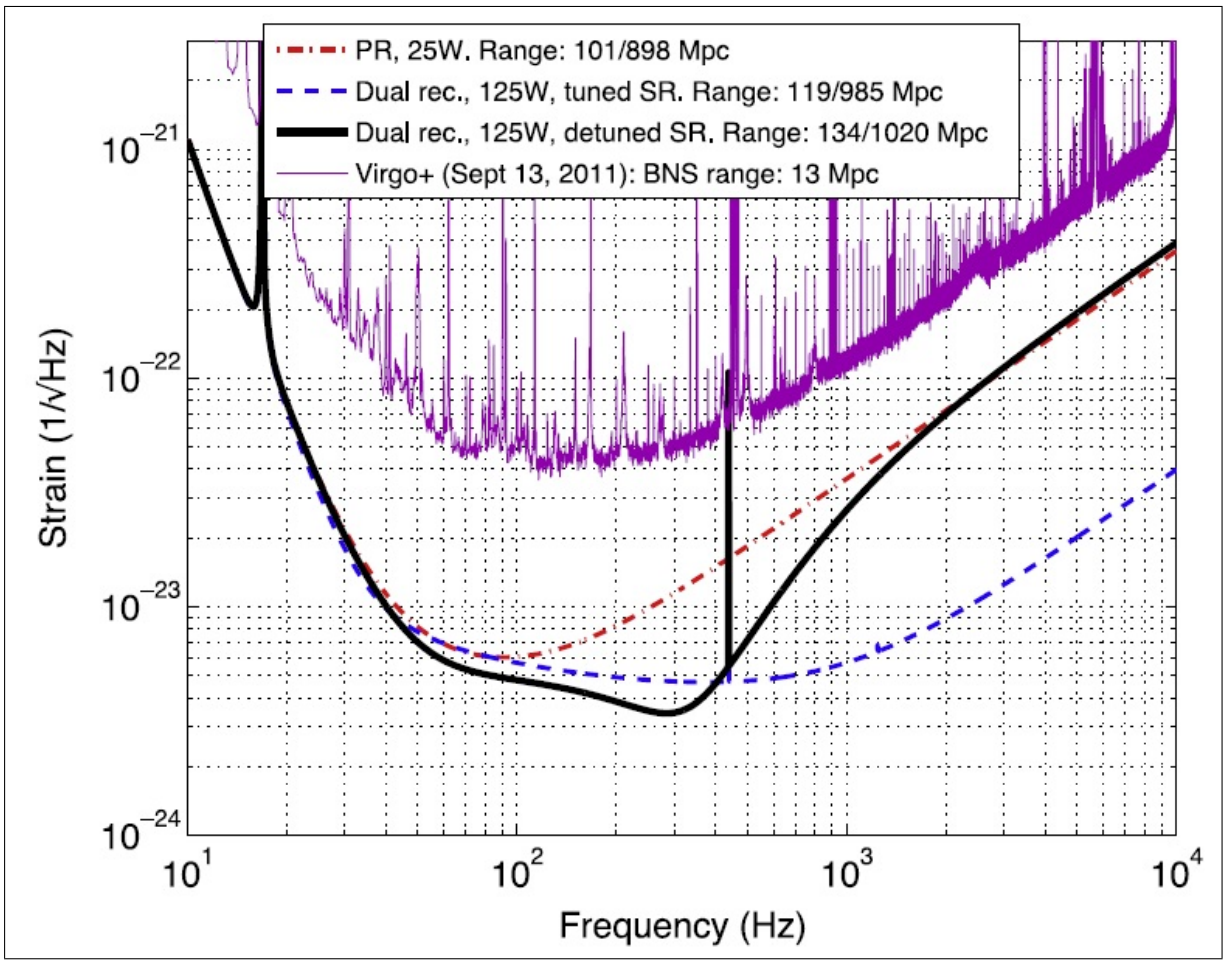

Figure 3.3: AdV sensitivity for the three different configurations: early operation (dash-dotted line), 25W input power, no signal recycling (SR); mid-term operation, wideband tuning (dashed line), 125W input power, tuned signal recycling; late operation, 125W input power, detuned signal recycling. The best sensitivity obtained with Virgo+ is shown for comparison. Figure taken from [14]

Chapter 4

The telescopes in Advanced Virgo

The main beam that illuminates the Virgo interferometer is a fundamental Gaussian beam. A Gaussian beam is fully characterized by 3 parameters: its beam waist w_0, the position of the latter, z_0, and its wavelength λ. Other properties can be defined, the Rayleigh length z_R and the divergence θ, as:

$$z_R = \frac{\pi w_0^2}{\lambda} \quad ; \quad \theta \simeq \frac{\lambda}{\pi w_0} \ . \tag{4.1}$$

The beam spot radius at a distance z from the waist position is given by:

$$w(z) = w_0 \sqrt{1 + \left(\frac{z}{z_R}\right)^2} \ . \tag{4.2}$$

Those parameters are depicted in 4.1.

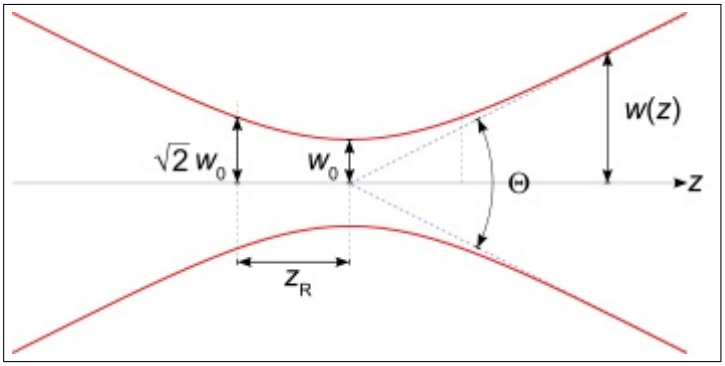

Figure 4.1: Gaussian beam parameters. Θ is defined as $\Theta = 2\theta$. Figure taken from [22]

After several z_R from the waist position, the beam can be considered as a spherical wave. Its radius of curvature is defined as:

$$R(z) = z \left[1 + \left(\frac{z_R}{z}\right)^2\right] . \tag{4.3}$$

Now, for such a beam to be resonant in a cavity, its waist needs to be unchanged after a loop in the cavity, therefore the radius of curvature of the beam has to be equal to the radius of curvature of the mirrors. For a fixed cavity, it means that the beam has to be tuned to match the cavity parameters. This can be done by using mode-matching telescopes.

4.1 Mode-matching telescopes in Advanced Virgo

Advanced Virgo contains two mode matching telescopes. One placed at the input of the interferometer, and the other one placed at the output [14]. The aim of the former is to adapt the beam properties to the ones of the arm cavities. The latter aims at reducing the dimension of the interference beam so that it could be collected at the output photodiodes. Figure 4.2 shows the position of those telescopes in Advanced Virgo.

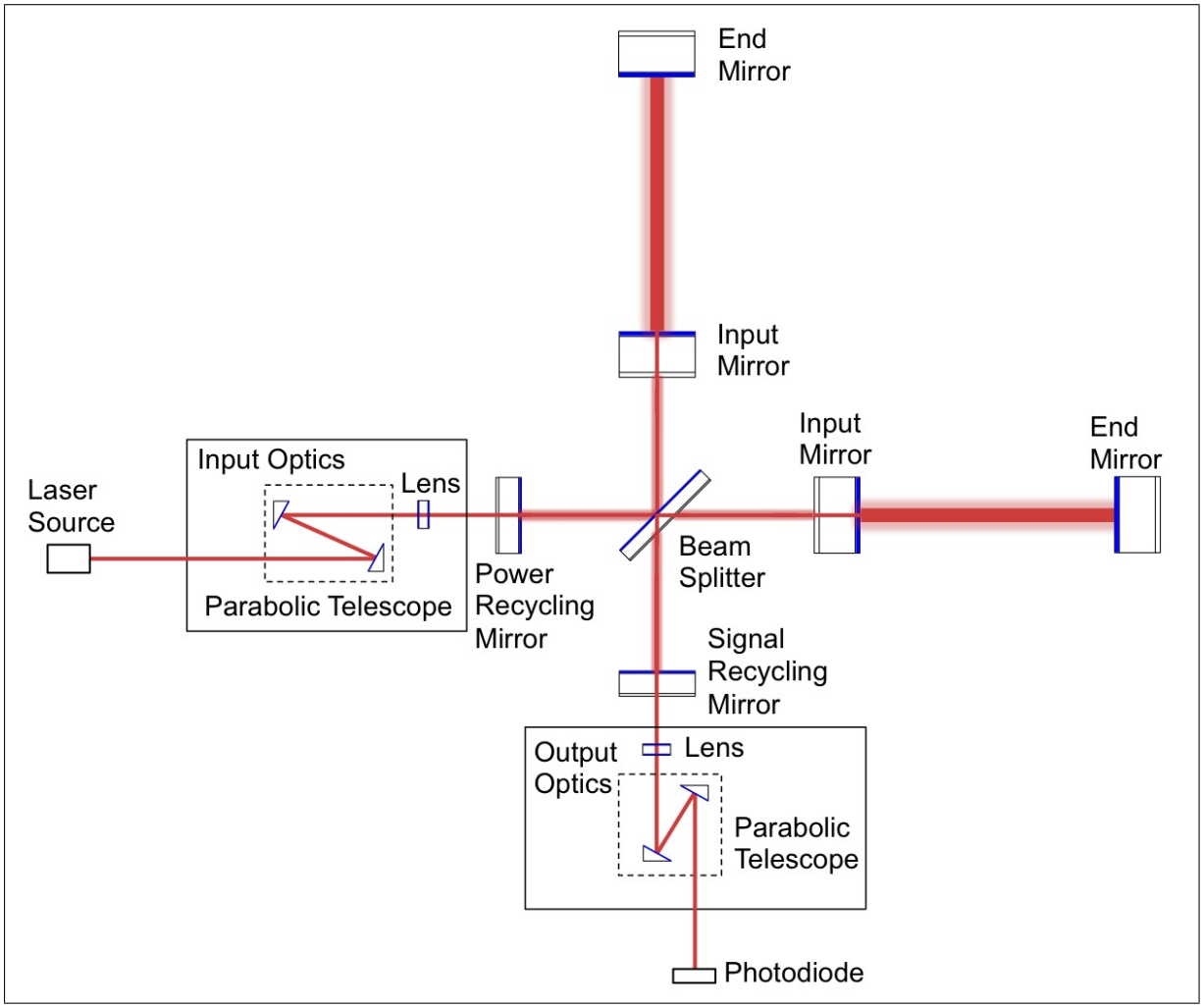

Figure 4.2: The two parabolic telescopes in Advanced Virgo.

The design of the mode-matching telescopes follows many requirements [17]. In particular, they have to provide a very large magnification, respectively a factor 19 for the input telescope and a factor 38 for the output one, filling in a small space (a maximum surface of 80x30 cm^2). Moreover the telescopes have to introduce negligible aberrations and provide beams with excellent wavefront quality: a theoretical matching with resonant cavities above 95 % and possibly $\sim$ 99 % is aimed for the beams given by the telescopes. The two telescopes are installed on optical benches that will be suspended in vacuum with a residual pressure of the order of 10^{-6} mbar. In addition, they will have to provide angular, longitudinal and transversal movements. That implies the installation of very accurate actuators, characterized by minimum incremental motion of the order of tens of nm, on the mechanical mounts.

4.2 Tuning of the output mode-matching telescope

The output mode-matching telescope contains two parts. A reflective part, which is an afocal off-axis parabolic telescopes formed by two mirrors $M1$ and $M2$, and a refractive part consisting in a meniscus lens L combined with the anti-reflective face of the signal recycling mirror. Figure 4.3 shows a scheme of the telescopes and figure 4.4 shows a picture of the output mode-matching telescope on its bench . The most critical part in the installation is the alignment of the reflective part. In an ideal configuration, the two axes of the parabolic mirrors should perfectly overlap. In addition the input beam should be perfectly align with those axes to minimize the aberrations.

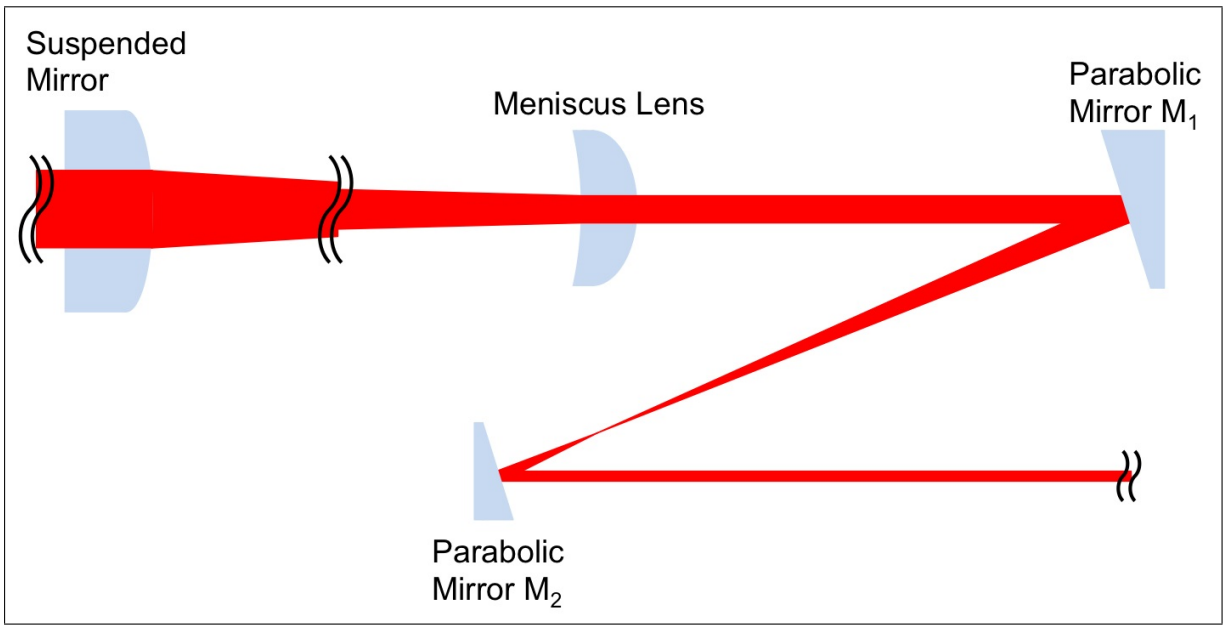

Figure 4.3: Optical layout of the mode-matching telescopes in Advanced Virgo.

4.2.1 Tuning procedure

Pre-alignment phase - It is decided to have the parabola axes perpendicular to one of the lateral surfaces of the optical bench. The angles of the two parabolic mirrors $M1$ and $M2$, both installed in gimbals mounts, are aligned using a reference mirror (RM) installed in two different positions on the side of the bench behind $M2$, i.e. about coaxially with respect to $M1$ (position $P1$) and $M2$ (position $P2$). The reference mirror mount lies on a clamp, which is machined to have the mirror surface parallel to the side surface of the bench. This allows RM to slide from $P1$ to $P2$ parallel to the bench edge.

The bench is rectified and, in addition, the reproducibility of RM angle when clamped to different positions on the bench side is verified: by observing the retro-reflection of two laser beams which have been aligned parallel to each other to better than 150 μrad, the mirror angle changes by less than 150 μrad.

As a first step a preliminary alignment of the telescope is performed: transverse mirror positions are measured with respect to reference points on the optical bench using a calliper; angular positions are aligned using the RM and two autocollimators.

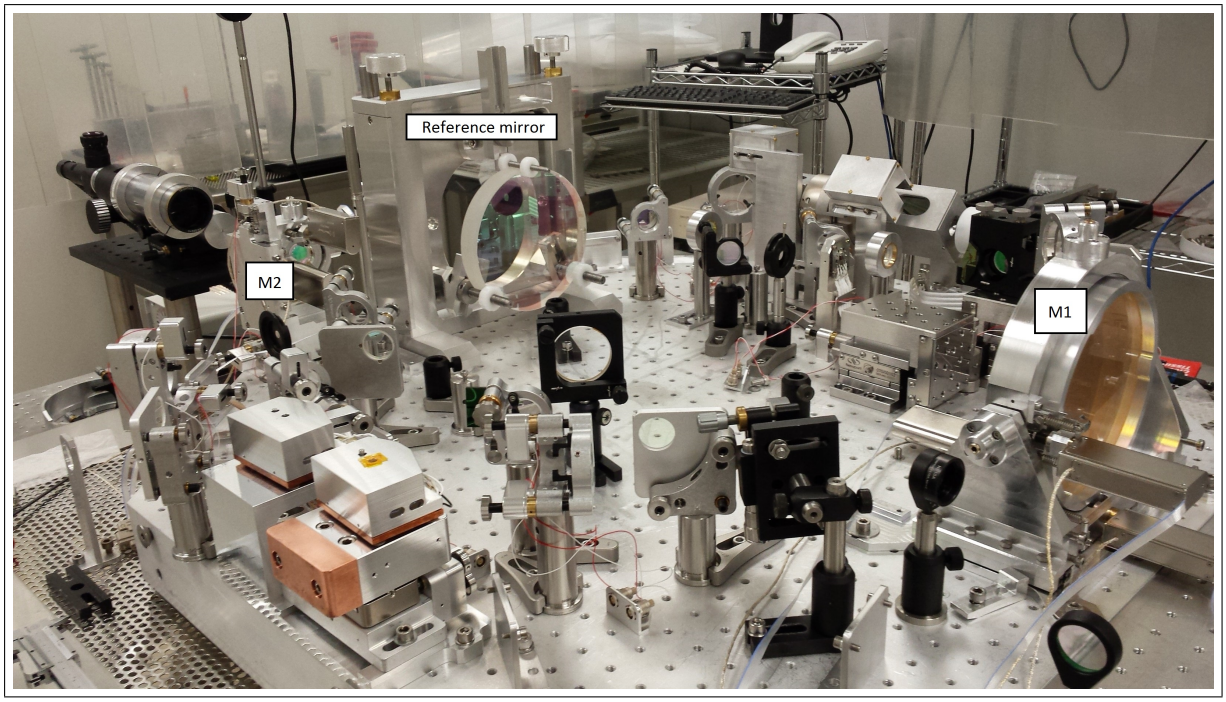

Figure 4.4: Picture of the output mode-matching telescope mounted on its bench in Advanced Virgo.

The transversal horizontal position of the two parabolic mirrors $M1$ and $M2$ with respect to the centre of the bench is determined by screwing some posts on the table and measuring the distances between the posts centres and the vertical gimbals axes of mirrors mounts. The uncertainty of the measurements is of the order of 200 μm, with nearly equal contributions from calliper precision, post positioning errors, and mechanical tolerances of mirror mounts.

Similarly, the transversal vertical position of both parabolic mirrors is determined by measuring the distance between the plane of the optical bench and the horizontal gimbals axes with a calliper. In addition, mirror rotation around the longitudinal axis is defined by reference marks provided by the manufacturer. The measurement uncertainty is of the order of 500 μm, dominated by the mirror rotation.

The telescope axis is parallel to the lines of threaded holes on the optical bench. The longitudinal distance between the two parabolic mirrors $M1$ and $M2$ is determined by measuring its projection along the telescope axis with some posts and a calliper. A post is placed in front of each mirror, at about the mirror centre, and the distance between the post centres and the vertical gimbals axes of the mirror mounts is measured. Then the distance between the two gimbals axes along the parabola axis is determined from the two measurements and the knowledge of holes spacing in the optical bench. The measurement uncertainty is of the order of 250 μm, with nearly equal contributions from calliper precision, post positioning errors, mechanical tolerances on bench holes machining and mechanical tolerances of mirror mounts.

The angular positions of the two parabolic mirrors are measured and adjusted with respect to the reference plane defined before with the help of two autocollimators (named $AC1$ and $AC2$). The procedure follows five successive steps, as described below and shown in figure 4.5.

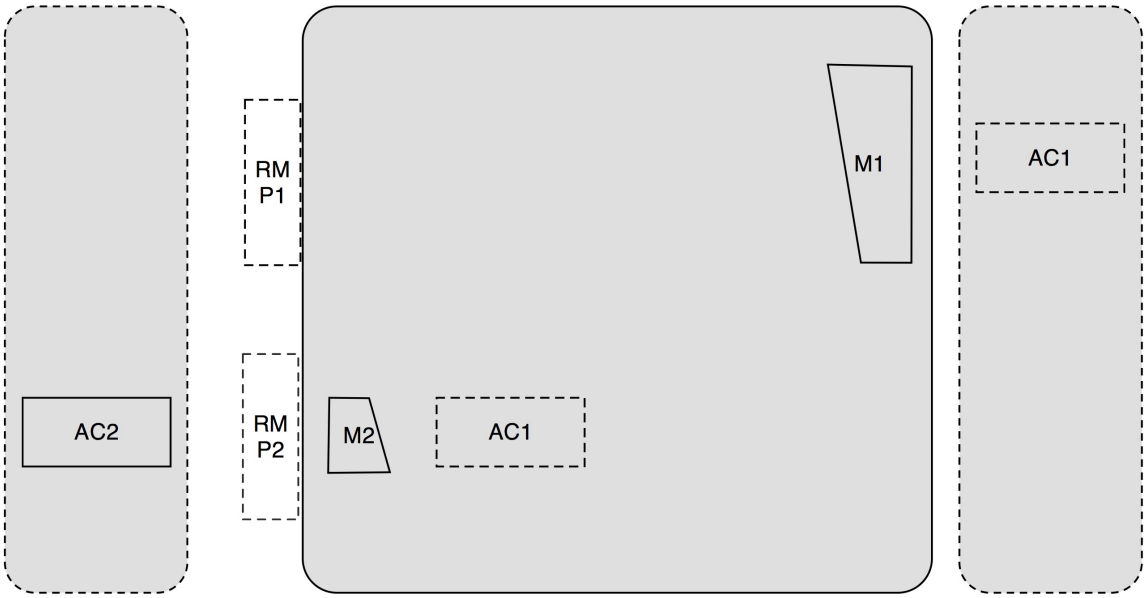

Figure 4.5: Set-up for the alignment of the angular degrees of freedom of $M1$ and $M2$ mirrors with autocollimators and a reference flat mirror.

- **Step 1:** The RM is clamped on the bench edge at position $P1$. $AC1$ is placed on an external, auxiliary bench just behind the nominal position of $M1$, then it is aligned with respect to the RM.
- **Step 2:** Mirror $M1$ is placed on the bench at its nominal positions. To this purpose the distances between the rotation centre of the mirror and some reference positions on the bench are measured, as described above, and the horizontal and vertical position of the mirror are tuned with the corresponding picomotors.
- **Step 3:** he angular position of the $M1$ mount is align by using the reflection of the flat back face of the parabolic mirror on the $AC1$, which was previously aligned with respect to the RM at step 1. It was required to the manufacturer to provide a polished and reflective mirror rear face parallel to the parabola vertex tangent plane.
- **Step 4:** $AC1$ is placed on the bench, just in front of the nominal position of $M2$. RM is clamped at position $P2$, i.e. in front of $AC1$, and the latter is aligned with respect to RM. RM is removed, $AC2$ is placed on a second external, auxiliary bench just behind the nominal position of $M2$, then $AC2$ is align with respect to $AC1$.
- **Step 5:** The parabolic mirror $M2$ is placed on its nominal position, with the same procedure described for $M1$ in Step 2, and it is aligned using the reflection of the back flat surface on $AC2$. Also the rear face of $M2$ is polished, reflective and parallel to the parabola vertex tangent plane.

Since the autocollimators feature a resolution of $150\,\mu$rad, the resulting uncertainty on the angular degrees of freedom is $250\,\mu$rad for $M1$ and $300\,\mu$rad for $M2$.

Fine-tuning phase - A small beam enters the telescope impinging on the the mirror $M2$. A reference mirror is placed in front of $M1$ so that the beam travels back through the telescope and is observed after $M2$. After a dual-pass, the beam, which is characterized by a small size, can be observed using standard wavefront sensors and cameras.

Since the input beam is perpendicular to the reference mirror, a non null angle between back-reflected and input beams indicates a misalignment of the telescope. The two beams can be superposed with a precision of 100 μrad by tweaking the angular degrees of freedom of either $M1$ or $M2$ and observing the back-reflected beam on a diaphragm centred on the input beam after an optical path of about 4 m from the reference mirror.

A method to obtain a good superposition of the two parabola axes consists in tuning the translational and angular degrees of freedom of one parabolic mirror while observing both the propagation direction and the shape of the back-reflected beam. In the ideal configuration of the telescope, the reflected beam must overlap with the input beam, it must be collimated and have no distortions. If a non null off-axis is compensated with a mirror tilt an astigmatic shape will appear on the reflected beam.

A beamsplitter is placed on the path of the input beam before $M2$ to pick off the retro-reflected beam and let it propagate for a distance of about 5 m after $M2$. We analyse the beam shape with a beam profiler and a wavefront sensor at three different positions: a few cm after the beam splitter, about 2.5 m after it and about 5 m after it. A scheme of the set-up is shown in figure 4.6. This allows us to determine the astigmatism and divergence of the back-reflected beam.

4.2.2 Figure of merit

In the ideal, afocal configuration, the telescope should not introduce any distortion to the laser beam mode. Given a TEM_{00} input beam, both the single-pass and the double-pass beams should provide a pure TEM_{00} mode.

In principle, residual distortions of the output beam can be described in terms of a set of parameters such as the astigmatism, the waist asymmetry, or the coefficients of Zernike polynomials. As a general figure of merit we take the overlap integral of the beam at the telescope output with an ideal Gaussian beam. We indicate by $I_t(r)$ the intensity distribution of the real laser beam at the output of the telescope, and by $I_g(r)$ the intensity distribution of a pure Gaussian laser beam. The overlap integral is then given by:

$$\eta = \frac{\iint I_t(r) \cdot I_g(r) dS}{\sqrt{\iint I_t^2(r) dS} \cdot \sqrt{\iint I_g^2(r) dS}} \tag{4.4}$$

4.2.3 Experimental results

The beam is observed for different distances after $M2$. Figure 4.7 shows the profile of the beam 5 m after $M2$ for different cases of misalignment.

The telescope is tuned following an iterative process to obtain a quite circular beam with dimensions similar to the input beam. Figure 4.8 shows a situation where the telescope is in a good alignment configuration. The output beam and the input beam are quite similar.

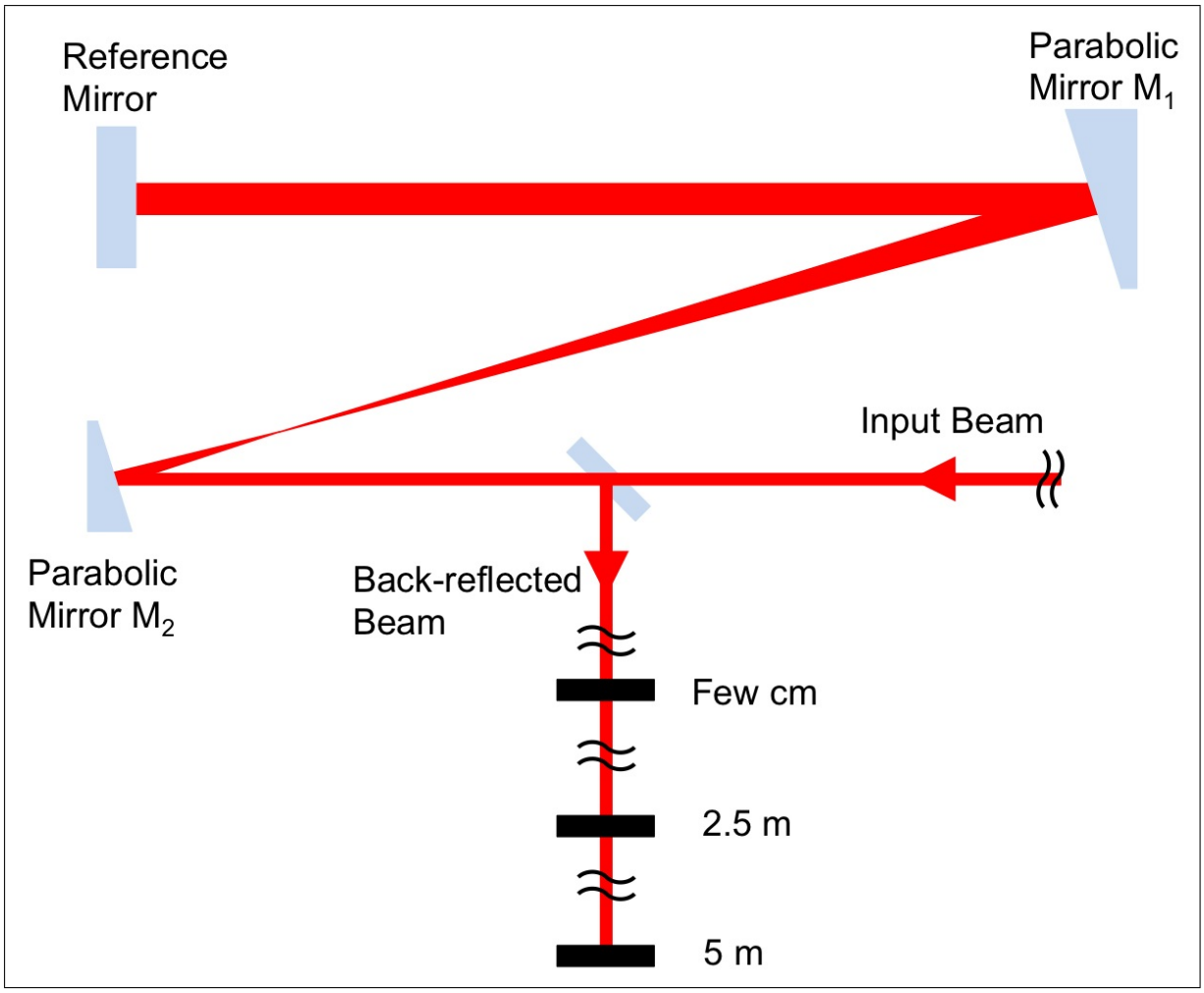

Figure 4.6: Scheme of the experimental set-up for the tuning procedure of the mode-matching telescope.

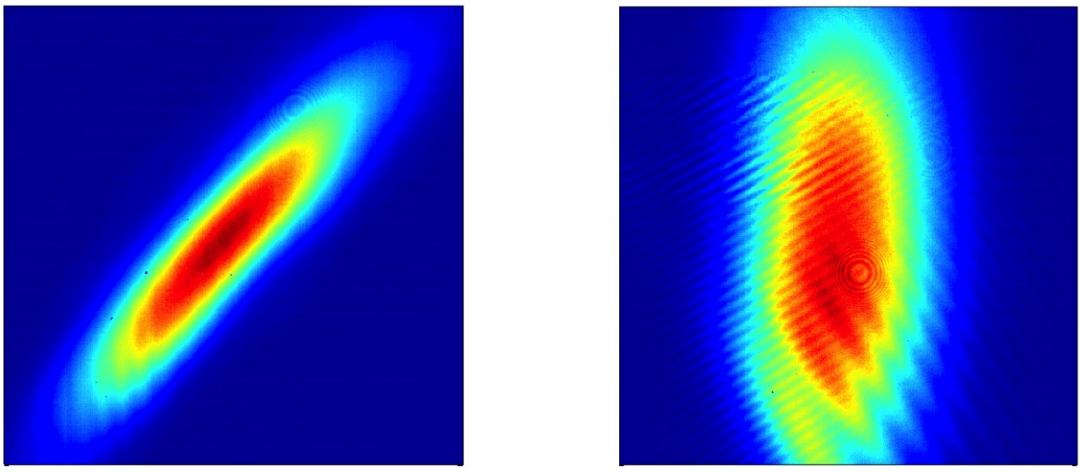

Figure 4.7: Back-reflected beam in presence of slight misalignment of the telescope: (a) non-perfect superposition of the parabola axes in horizontal and vertical direction, (b) wrong horizontal off-axis.

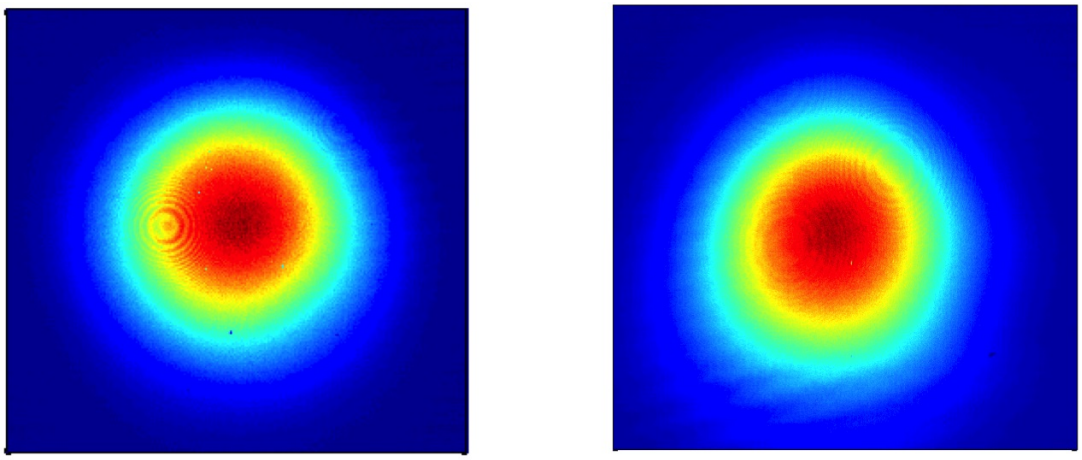

Figure 4.8: (a) Beam at the input of the telescope; (b) Back-reflected beam in a good alignment configuration.

After obtaining a situation where the output beam is quite circular, meaning that the parabola axes are quite superposed, the beam parameters are measured for different longitudinal positions of $M1$ in order to obtain the dimensions that maximize the overlap integral η of eq. 4.4. Figure 4.9 shows the different measured parameters (the beam waist and the waist position) for the different longitudinal positions.

This allows to identify the longitudinal offset with respect to the nominal longitudinal position of $M1$ that gives the best matching: $0.6 \pm 0.1\ mm$. By approaching this configuration, a matching of $\eta = 98\%$ has been achieved.

4.3 Errors simulation

The output mode-matching telescope, along with its bench, will be suspended in vacuum. During this procedure, a small detuning of the telescope is to be expected. In order to anticipate the consequences of such possible detuning, a simulation of the possible errors is achieved.

4.3.1 Single error analysis

Method Using ZEMAX [18], we model the output mode-matching telescope in its real working configuration: single-pass from the meniscus lens to the mirror $M2$. The beam will be observed two meters after the $M2$ mirror. The measured parameters are the position of the beam in the transversal (X,Y) plane, the beam spot size in the transversal X and Y directions, and the waist and waist position. The coupling with an ideal Gaussian beam can then be computed using the waist and waist position through Matlab.

We limit the analysis to displacements of the beam $< \pm 5\ mm$ and beam spot size variation $< \pm 350\ \mu m$.

The simulation configuration and reference beam are presented in 4.10.

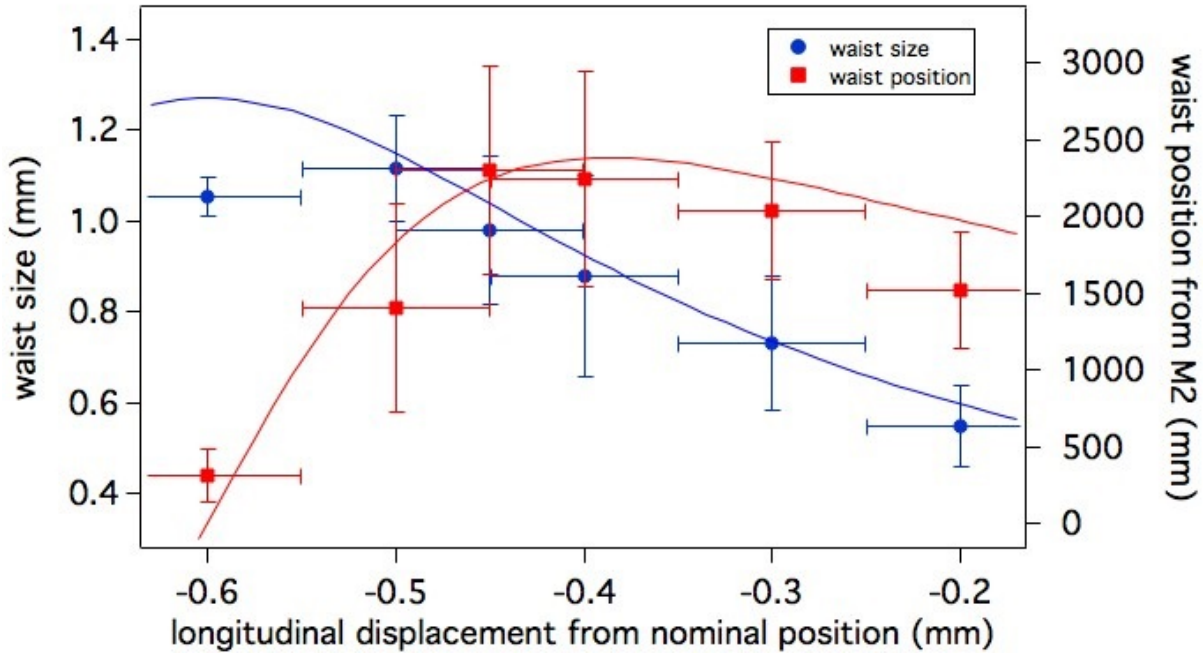

Figure 4.9: Waist radius w_0 and waist position z_0 versus the longitudinal position z_l of $M1$. The zero in the horizontal scale corresponds to the nominal position. Circles and squares are experimental data; error bars are from least-squares fit made with equation (4.2); solid lines are values from the numerical simulation. An offset of $-0.6\,\text{mm}$ has been applied to the horizontal scale of the simulation, in order to match the experimental data.

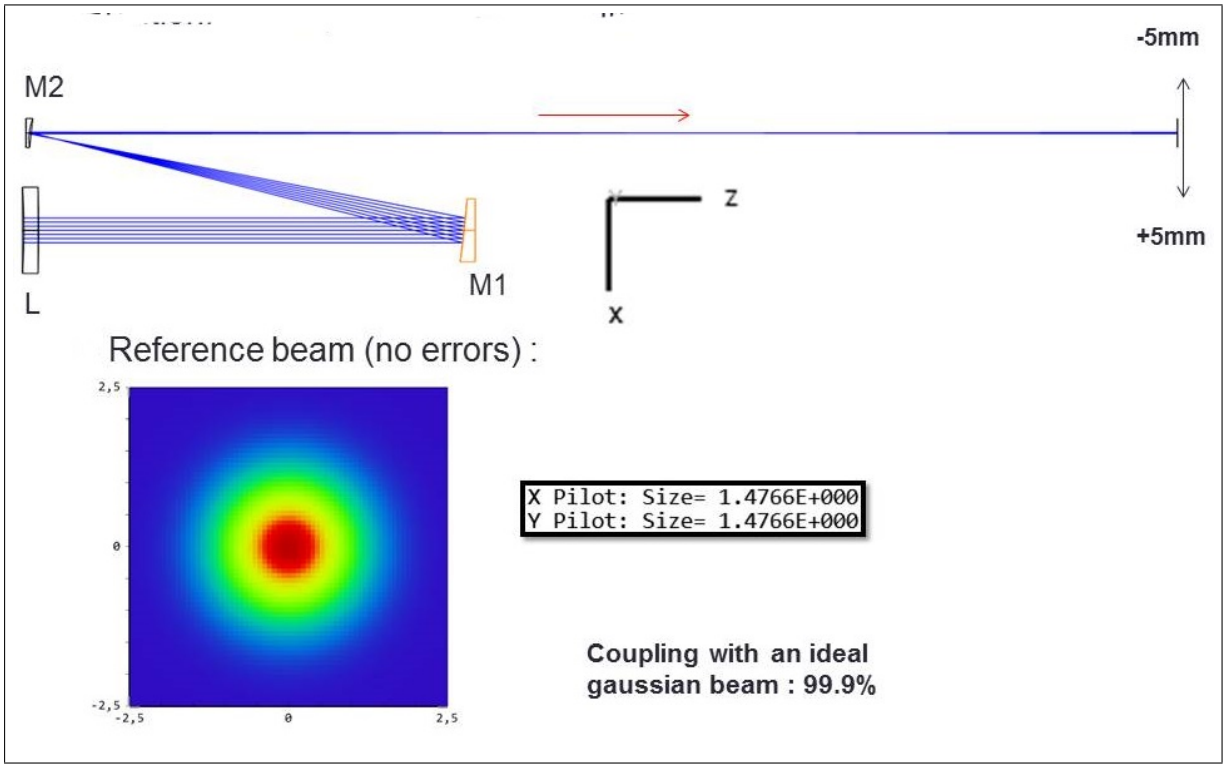

Figure 4.10: The simulation configuration and the reference beam parameters at the point of observation with an illustration of the beam relative intensity profile.

Analysis First, for each degree of freedom, the beam displacement in the (X,Y) plane and the beam size along X and Y are plotted as functions of the error on the degree of freedom, in the range of the analysis. Figure 4.11 shows an example of such curves. The X and Y positions of the beam are plotted as function of the error on the $M1$ mirror angular position around the x-axis, θ_x.

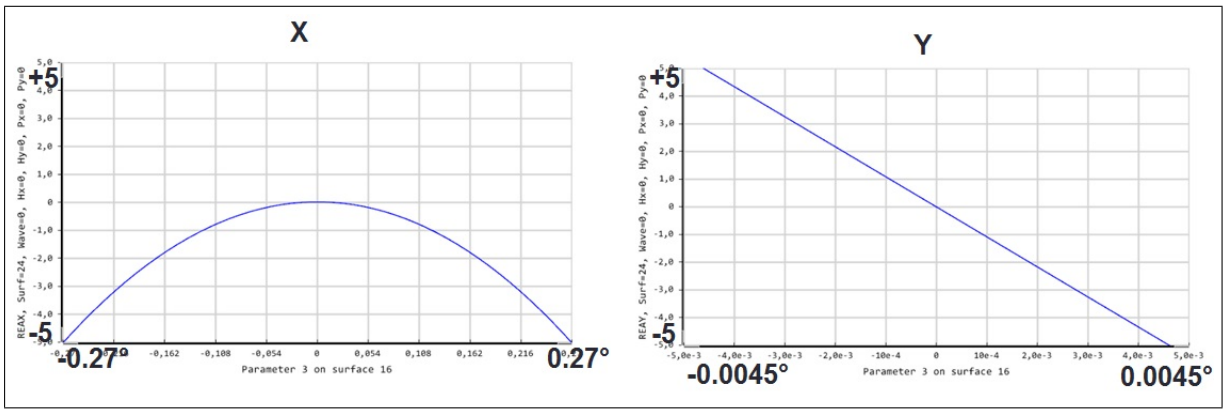

Figure 4.11: Plot of the beam X and Y position as functions of the error on $M1$ θ_x angular position.

Then, for each degree of freedom, the value of the error on this degree of freedom that makes the beam parameters goes to the analysis limits (the value of the error that makes the beam position drift to ± 5 mm for example) is noted.

Finally, the value of each error on the degrees of freedom that makes the coupling with an ideal Gaussian beam goes to 95% is noted.

Results All the previous errors values are listed in table 4.1. For each value, a beam spot relative intensity profile is available. Figure 4.12 shows example of such profiles. The coupling on the OMC is also computed for each value.

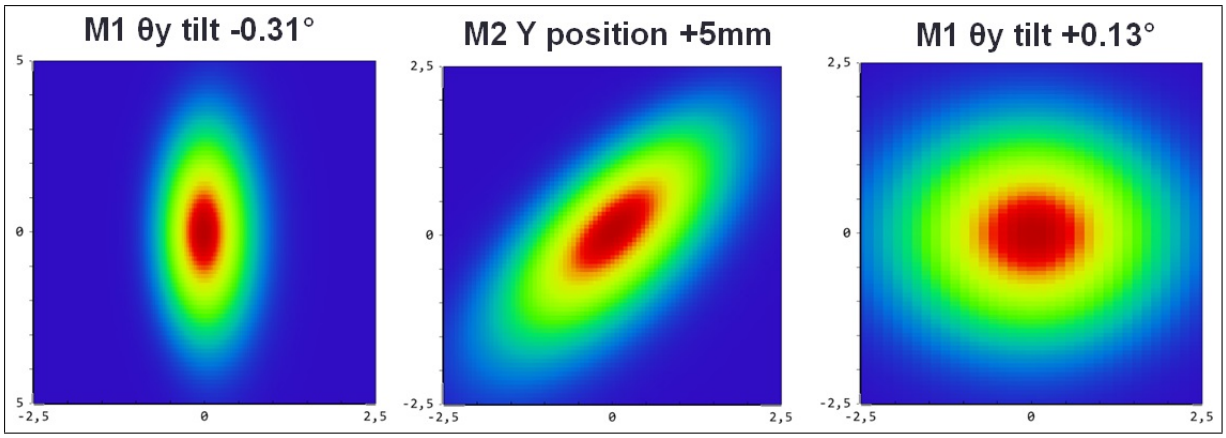

Figure 4.12: Example of the beam relative intensity profile for different errors.

Conclusions The obtained results lead to the following conclusions:

- Except for the longitudinal position of M1, the beam is always good (coupling $> 99\%$) in the range ± 5 mm.

			Errors Limits								coupling 95%	
			X-Position		Y-position		wx		wy			
Mirror	error type	Direction	+5mm	-5mm	+5mm	-5mm	+350µm	-350µm	+350µm	-350µm	<0	>0
M1	position (mm)	Z	0,55	-0,55	Ø	Ø	-0,3	0,33	-0,3	0,33	**-0,26**	**0,23**
M1	tilt (mrad)	X	Ø	± 4,7	-0,08	0,08	± 3,5	Ø	± 3,5	Ø	**-2,6**	**2,6**
M1	tilt (mrad)	Y	-0,08	0,08	Ø	Ø	1,0	-1,6	-5,4 / 2,3	Ø	**-2,3**	**1,4**
M2	position (mm)	X	0,12	-0,12	Ø	Ø	0,8	-1	-12 / 2,2	-5 (min)	**-1**	**1,1**
M2	position (mm)	Y	Ø	Ø	-0,12	0,12	± 5	Ø	± 5	Ø	**-2,15**	**2,15**
M2	tilt (mrad)	X	Ø	± 148,4	-2,6	2,6	± 106,5	Ø	Ø	± 118,7	**-48,0**	**48,0**
M2	tilt (mrad)	Y	-2,6	2,6	Ø	Ø	19,2	-19,2	-275,8 / 47,1	-113,4 (min)	**-20,9**	**26,2**

Table 4.1: Errors analysis results. The highlighted values are the most critical values for each error.

- Large errors are needed to worsen the quality of the beam: errors that make the coupling with an ideal Gaussian beam are larger than what is expected to be possible.
- Except for the longitudinal position of M1, the beam deformation is always elliptical (astigmatism).
- The most critical errors are the two tilts of M1.

In the future suspension of the bench inside the vacuum tower, a particular attention will then have to be paid on the $M1$ mirror angular positions.

4.3.2 Coupled errors analysis

The effect of errors applied to two different degrees of freedom at the same time is also studied. In particular, the possibility that two errors can compensate their effect on the beam quality and position is evaluated. It appears that a couple of errors never has the same effect on both the quality and the beam position. An example of this analysis is shown in figure 4.13. Considering a Gaussian beam of waist $w = 1.470\,\text{mm}$ and inducing an error on $M1$ yaw angular position of $+0.045\,\text{deg.}$ and an error of about $-0.6\,\text{mm}$ on the horizontal off-axis distance between the two mirrors, the effects on the beam size compensate each other (points specified in figures 4.13(a) and 4.13(b)) so that the beam shown in figure 4.13(c) is obtained at the output of the telescope and an overlap integral with an ideal Gaussian beam of 99.9% is achieved. However, the effects on the beam

position lead to a shift along x of about +24 mm at a distance of 2 m from $M2$ with respect to the nominal one, as shown in figure 4.13(d). This shift corresponds to a beam deflection of 12 mrad; in many practical cases, e.g. in the Advanced Virgo telescopes, such a large tilt would produce unacceptable misalignment of the beam on the optical components after the telescope output.

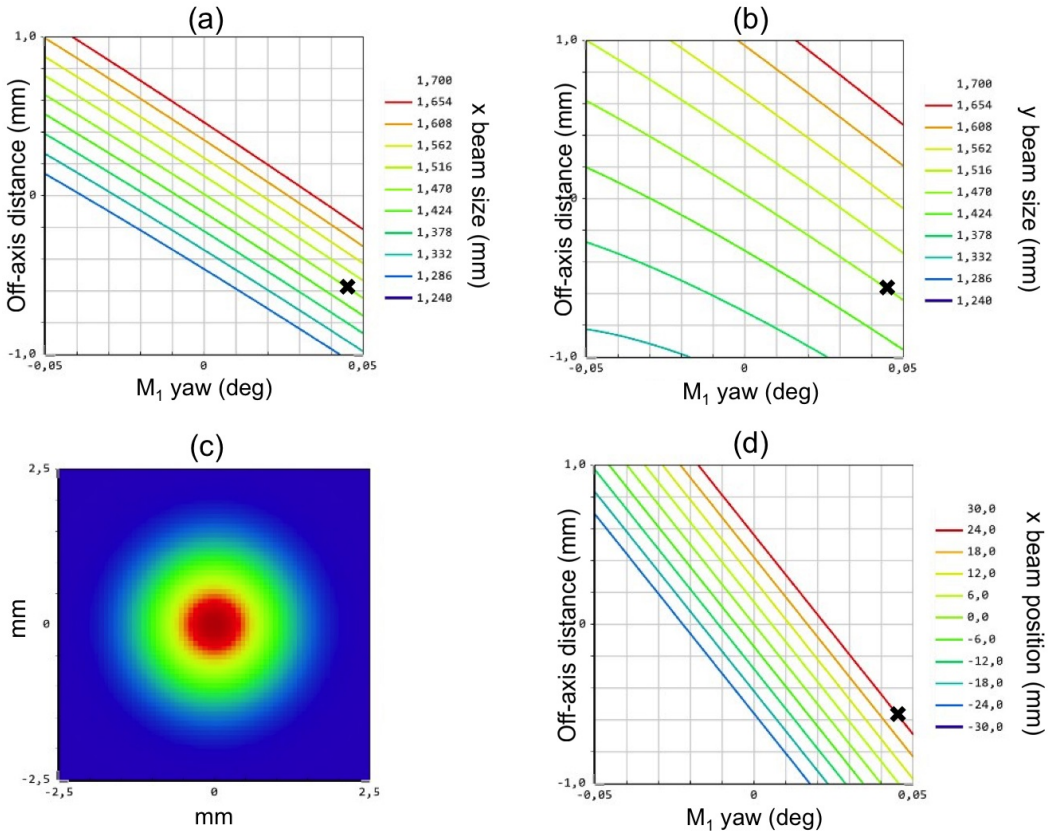

Figure 4.13: Effect of errors on the $M1$ yaw angular position and on the off-axis distance: (a) trend of the beam size along the horizontal direction; (b) trend of the size along the vertical direction; (c) image of the beam shape in the configuration indicated with a cross in the plots; (d) horizontal position of the beam at a distance of 2 m from $M2$ (results obtained with ZEMAX [18] simulations).

4.3.3 Experimental results validation: single-pass configuration vs double-pass configuration.

The experimental measurement performed on the output mode-matching telescope has been carried out in a double-pass configuration. The laser beam undergoes two reflection on each mirrors, thus the possible aberrations due to misalignment are introduced twice. Therefore, the resulting deviation from a ideal Gaussian beam is expected to be amplified in such a configuration.

In order to validate this expectation, it is decided to compare the computed values of the coupling with an ideal Gaussian beam in a single-pass configuration (the one of Advanced Virgo, used in the previously described simulations) and in a double-pass configuration.

Procedure - For three different errors (longitudinal position of $M1$, off-axis position of $M2$ and $M1$ pitch) we simulate the beam profile after a double-pass in the the telescope. The overlap integral with a ideal Gaussian beam is then computed and compared to the value obtained previously, in a single-pass configuration. The results are showed in figure 4.14.

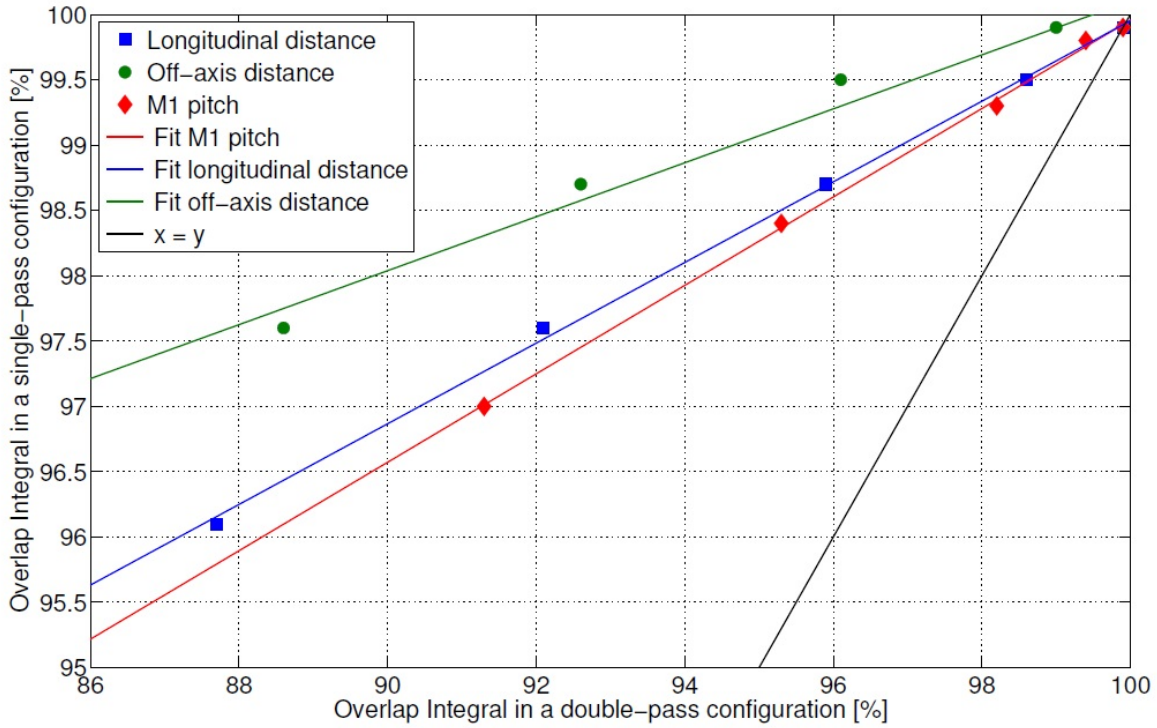

Figure 4.14: Overlap Integral in a single pass configuration vs. Overlap integral in a double-pass configuration for different amplitude of different errors (blue curve = longitudinal distance between the two mirrors; green curve = off-axis distance between the two mirrors; red curve = $M1$ pitch angle).

It appears that the points are all over the $x = y$ line, which confirm the hypothesis. The coupling with an ideal Gaussian beam is better in a single-pass configuration than in a double-pass configuration. The measurement of this coupling in a double-pass configuration is thus relevant.

4.4 Wavefront sensor and cavity experiment

In Advanced Virgo, the beam coming out of the output telescope will be matched inside an output mode-cleaner cavity. Two more lenses are needed to obtain the right beam parameters. In order to check the effect of different configurations of the parabolic telescope, in particular the longitudinal distance between the two mirrors, an experiment has been implemented in laboratory.

4.4.1 Experimental setup

The experimental set-up consist of an off-axis parabolic afocal telescope and a plano-concave Fabry-Pérot cavity in series. A first pair of lenses is used to select the dimension of the beam that enters the telescope. A second pair of lenses, placed between the telescope and the cavity, allows to tune the beam to achieve the matching on the cavity. The telescope is composed by two parabolic mirrors $M1$ and $M2$, like the telescopes in Advanced Virgo. The beam is divided in two at the output of the parabolic telescope: the first beam is acquired with a wavefront sensor, while the other one is matched on the cavity. The optical layout is shown in figure 4.15 and figure 4.16 shows a picture of the experiment in the laboratory.

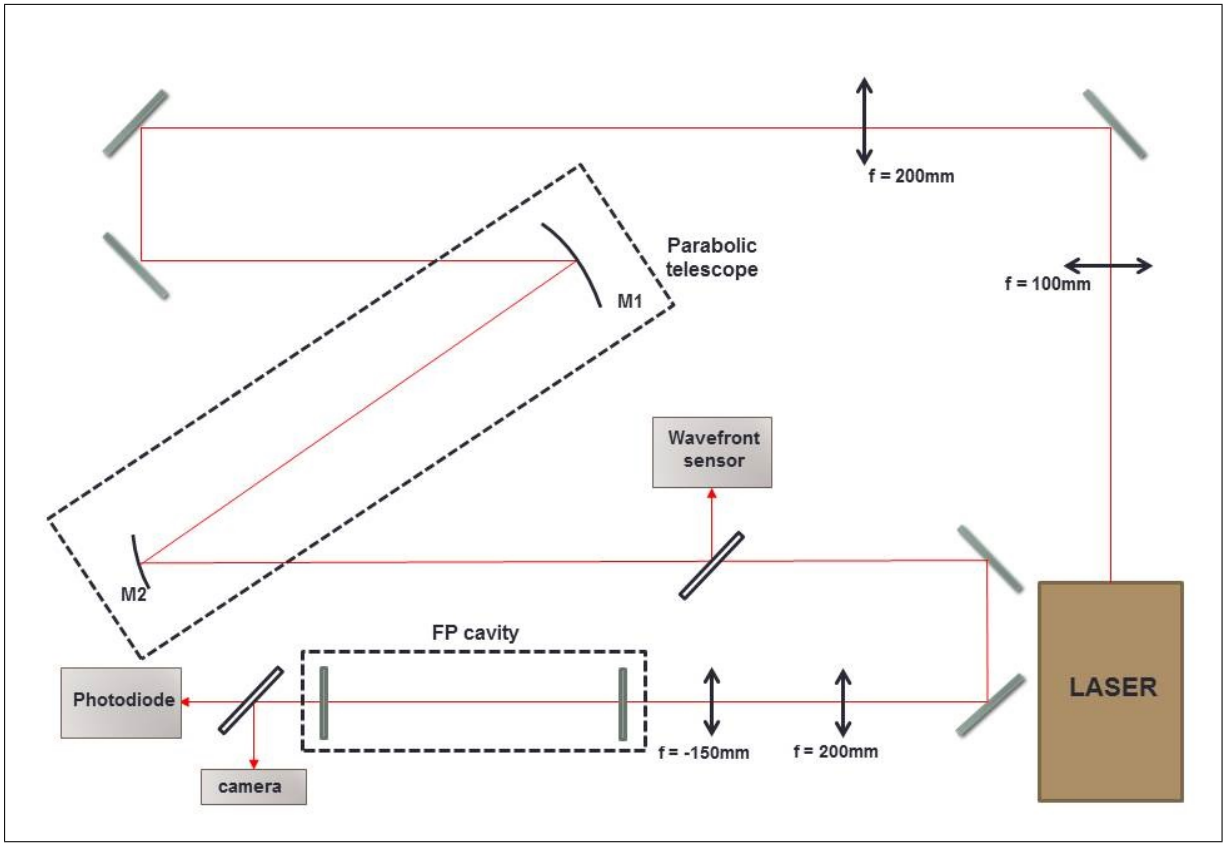

Figure 4.15: Optical layout of the experiment.

4.4.2 Tuning procedure

Tuning of the telescope First, the two mirrors are placed in their nominal positions and the output beam is aligned. The wavefront sensor placed at the output of the telescope, about 120 cm behind $M2$, acquires the output beam. The next step consists in superposing the axes of the parabolic mirrors by tuning the different degrees of freedom on $M1$. This gives an opportunity to validate and exploit the results of the performed simulations. The profile of the acquired beam can indeed be compared to the simulated profiles and the errors can be qualitatively identified, so that one knows what degree of freedom has to be tuned.

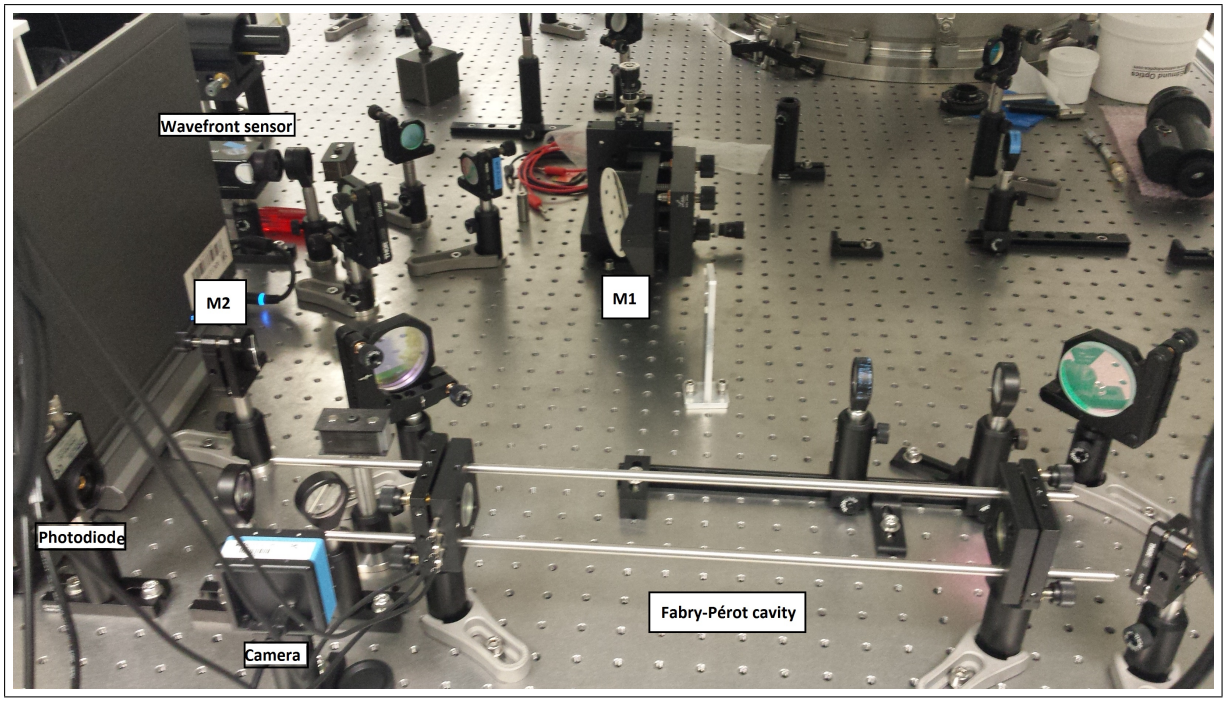

Figure 4.16: Picture of the experiment in the laboratory.

This is what practically happened: the tuning procedure had been quite simplified by the simulations results. The experiment is in agreement with the simulations. Figure 4.17 shows the acquired beam profile before the tuning procedure (left) and the simulated profile when an error on the $M1$ roll (θ_x) in introduced. This allows to tell that the main source of misalignment in the experiment is the roll of $M1$. This is only a qualitative comparison, since the simulations concern a system with different parameters!

Figure 4.18 shows the beam profile before and after the tuning procedure: at the beginning the beam is slightly astigmatic, while at the end of the procedure it is well circular.

Tuning of the Fabry-Pérot cavity First, the two needed lenses are determined by numerical simulation in order to obtain a beam that will match the cavity.

The end mirror of the cavity is mounted on a piezoelectric. This allows to modify the cavity length periodically to scan the different resonant modes. Two modes are used in the experiment: the fundamental Gaussian mode (TEM_{00}) and the mode of matching, which is a Laguerre-Gauss mode (LG_{01}). All the other modes are due to the misalignment of the cavity. Tuning the different degrees of freedom on the cavity mounts allows to get rid of them.

4.4.3 Mode-matching experimental results

The cavity is scanned using the piezoelectric mount and the output signal of the photodiode, which is expressed in terms of Volts and is directly proportional to the optical power, is plotted as a function of time. Each resonant mode in the cavity appears as a peak on the plot. A camera acquires the image in parallel, so that each mode can be identified. The ratio between the power of the matching mode LG_{01} and the fundamental

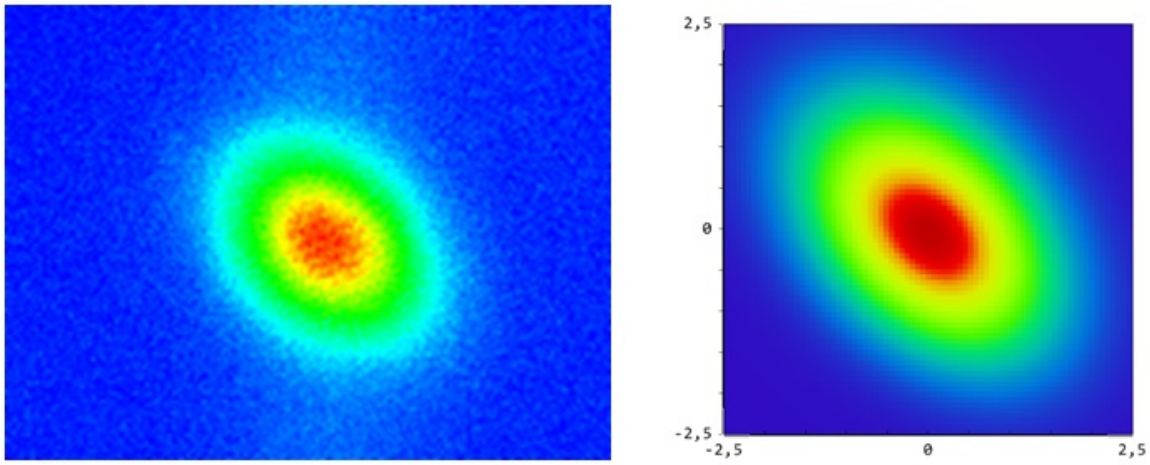

Figure 4.17: Acquired beam profile (left) and simulated beam profile when an error on $M1$ roll (θ_x) is introduced. (right)

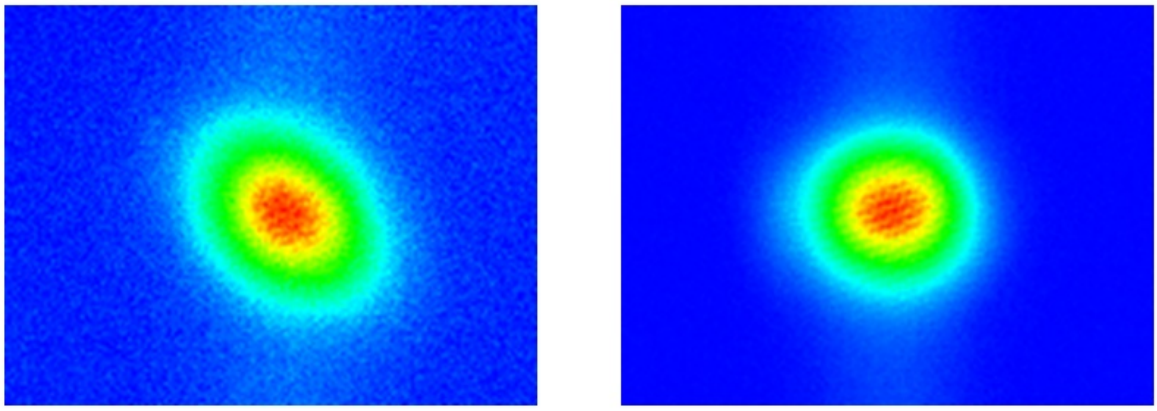

Figure 4.18: Beam profile before (left) and after (right) tuning procedure.

Gaussian mode TEM_{00} modes is chosen as a figure of merit to evaluate quantitatively the quality of the matching. The closer it is to zero, the better is the matching. Figure 4.19 shows these two modes.

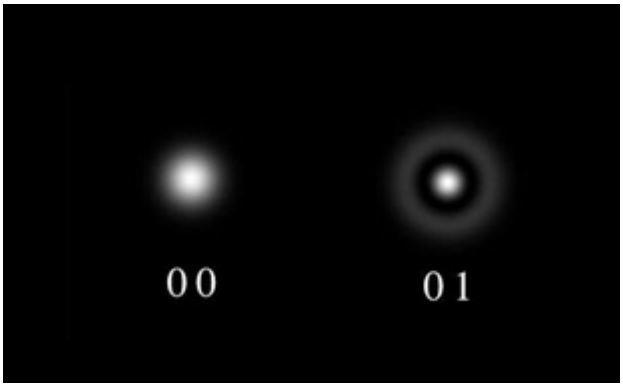

Figure 4.19: The TEM_{00} (left) and LG_{01} (right) modes. Figure taken from [22]

Figure 4.20 shows the output signal of the photodiode when the parabolic telescope is its reference position. The two peaks have been identified and the quality factor is in this case $1.3\% \pm 0.1\%$.

When the longitudinal distance between the two mirrors of the parabolic telescope is increased by 500 μm, the quality factor goes to $1.5\% \pm 0.1\%$. When it is decreased by 500 μm, the quality factor goes to $2.9\% \pm 0.1\%$. However, in three different position, the beam parameters measured at the wavefront sensor stay relatively unchanged. For example the beam radius at the wavefront sensor remains 2.0 ± 0.1 mm.

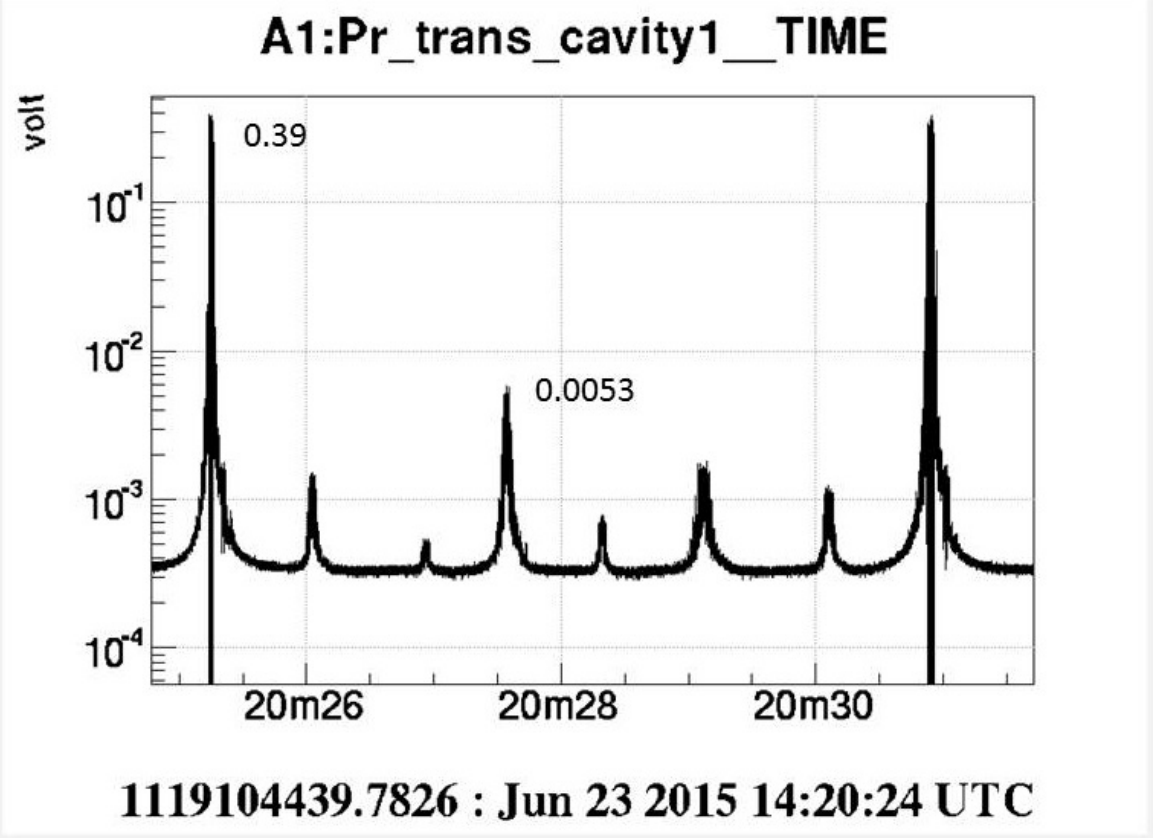

Figure 4.20: Output signal of the photodiode during the scanning of the cavity. The peak on the left is the TEM_{00} while the one on the right is the LG_{01}. The corresponding quality factor is $1.3\% \pm 0.1\%$.

Chapter 5

Conclusion

Advanced Virgo is a second generation gravitational waves interferometric detector. Its design requires the implementation of compact off-axis parabolic telescopes. My work has been dedicated to the installation and the characterization of the output mode-matching telescope, which aims at reducing the beam dimension and achieving a good matching with the output mode-cleaner cavity.

The output mode-matching telescope has been well aligned, so that a coupling of 98% with an ideal Gaussian beam has been achieved. This had been possible thanks to the particular alignment method that had been developed.

This procedure has been followed by numerical simulations in order to better predict the behaviour of the telescope after it is suspended under vacuum. These simulations give qualitative and quantitative information on the consequences of every errors on each degrees of freedom of the two parabolic mirrors. It has been shown that the most critical errors are the angular ones of $M1$. Thus, a particular attention will have to be paid to the tuning of $M1$ after the bench is suspended since errors due to the suspension and vacuum procedure might be large enough to deteriorate the beam position and quality. The fact that two different errors cannot compensate both the position and quality errors on the beam has also been shown. The alignment procedure and the simulations results will be presented in a scientific paper to be submitted soon [19].

Finally, an experiment has been performed in the laboratory to observe the behaviour of a wavefront sensor and of a Fabry-Pérot cavity when the longitudinal distance between the two parabolic mirrors varies. In particular, the beam transmitted by the cavity has been acquired to analyse the scan of the various modes that resonate in the cavity. The result was that the matching on the cavity deteriorates, but it is not clearly visible on the wavefront sensor. As a consequence, attention will have to be paid to the scan of the output mode-cleaner cavity, since the wavefront sensor alone will not be sufficient to evaluate the quality of the matching.

Chapter 6

Acknowledgement

I want first to express my sincere gratitude to Matteo Tacca for all the time he has dedicated to my thesis, for his constant support and for his precious advice.

I want to thank Matteo Barsuglia for the trust he has given to my work and for all his support, and Christelle Buy for helping me when needed. I am also grateful to Eric Bréelle for his help and for our pleasant and useful discussions on the wide world of scientific research.

Finally, I would like to thank all the members of APC and of the EGO group that I had the chance to meet for their kindness and their warm welcome.

List of Figures

List of Tables

Bibliography

[1] M. Maggiore, *Gravitational Waves. Vol. 1: Theory and Experiments*, Oxford University Press, Oxford, 2007.

[2] P. R. Saulson, *Fundamentals of Interferometric Gravitational Wave Detectors*, World Scientific, Singapore, 1994.

[3] D. G. Blair (ed.), *The Detection of Gravitational Waves*, Cambridge University Press, Cambridge, 1991.

[4] D. G. Blair (ed.), et al., *Advanced Gravitational Wave Detectors*, Cambridge University Press, Cambridge, 2012.

[5] M. Bassan (ed.), *Advanced Interferometers and the Search for Gravitational Waves*, Springer, Switzerland, 2014.

[6] F. Acernese et al. (Virgo Collaboration), Classical Quantum Gravity, 25, 184001, 2008.

[7] B.P. Abbott et al. (LIGO Scientific Collaboration), Rep. Prog. Phys. 72, 076901, 2009.

[8] M. Barsuglia et al., Virgo Internal Note VIR-0010B-12, 2012.

[9] A. Einstein, *Die Grundlage der allgemeinen Relativitätstheorie*, Annalen der Physik 354, 769 (1916)

[10] M. Maggiore, *Gravitational wave experiments and early universe cosmology*, Phys. Rep. 331, 283 (2000)

[11] A. Abramovici et al., *LIGO: The Laser Interferometer Gravitational-Wave Observatory*, Science 256, 325 (1992)

[12] C. Bradaschia et al., *The VIRGO Project: A wide band antenna for gravitational wave detection*, Nucl. Instrum. Meth. A 289, 518 (1990)

[13] B. Willke, N. Uehara, E. K. Gustafson, R. L. Byer, E. L. Ginzton, P. J. King, S. U. Seel and R. L. Savage Jr., *Spatial and temporal altering of a 10-W Nd:YAG laser with a Fabry-Perot ring-cavity premode cleaner*, Opt. Lett. 23, 1704 (1998)

[14] F. Acernese et al. (Virgo Collaboration), Class. Quantum Grav., 32, 024001, 2015.

[15] The LIGO Scientific Collaboration, *Advanced LIGO*, Class. Quantum Grav. 32 074001 (2015).

[16] J. Aasi et al. (LIGO Scientific Collaboration and Virgo Collaboration), arXiv:1304.0670v1, 2013.

[17] C. Buy, E. Genin, M. Barsuglia, R. Gouaty, M. Tacca, *Design of a high-magnification and low-aberration compact catadioptric telescope for Advanced Virgo laser interferometer*, Paper in preparation.

[18] M. Tacca, F. Sorrentino, C. Buy, M. Laporte, G. Pillant, E. Genin, P. La Penna and M. Barsuglia, *Tuning of a high magnification and low aberration compact parabolic telescope for cm-scale laser beams* (to be submitted).

[19] ttp://www.zemax.com

[20] http://www.ligo.org/science/GW-Inspiral.php

[21] https://inspirehep.net/record/1223270/plots

[22] https://en.wikipedia.org/wiki/Gaussian_beam